HARVARD
Kenneth C. Griffin

GRADUATE SCHOOL
OF ARTS AND SCIENCES

THESIS ACCEPTANCE CERTIFICATE

The undersigned, appointed by the

Department of Physics

have examined a dissertation entitled

Exploring 2D Quantum and Acoustic Systems Using Scanning Probes

presented by Benjamin November

candidate for the degree of Doctor of Philosophy and hereby certify that it is worthy of acceptance.

Signature _____

Typed name: Prof. Jenny Hoffman

Signature _____

Typed name: Prof. Philip Kim

Signature _____

Typed name: Prof. Ashvin Vishwanath

Date: March 28, 2025

Exploring 2D Quantum and Acoustic Systems Using Scanning Probes

A DISSERTATION PRESENTED
BY
BENJAMIN NOVEMBER
TO
THE DEPARTMENT OF PHYSICS

IN PARTIAL FULFILLMENT OF THE REQUIREMENTS
FOR THE DEGREE OF
DOCTOR OF PHILOSOPHY
IN THE SUBJECT OF
CONDENSED MATTER PHYSICS

HARVARD UNIVERSITY
CAMBRIDGE, MASSACHUSETTS

MARCH 28, 2025

Thesis advisor: Professor Jennifer E. Hoffman Benjamin November

Exploring 2D Quantum and Acoustic Systems Using Scanning Probes

Abstract

The world of quantum materials is made rich by the coexistence of many, many interacting electrons, giving rise to complex and fascinating phases of matter such as topological superconductivity. Such emergent quantum phenomena are associated with small interaction energy scales, appearing only in specific materials at ultra low temperatures. In this thesis I will address two distinct pathways towards studying strongly correlated materials: 1) creating better instrumentation and 2) discovering new materials.

In order to study already existing quantum materials, and more specifically topological superconductors, I will present the design and construction of a mK-base temperature scanning probe microscope. This system is the first of its kind to support simultaneous scanning tunneling microscopy and optical detection pendulum atomic force microscopy at mK temperatures. Such a combination opens the door for the realization of my proposed topologically protected quantum logic operation in the topological superconductors.

An alternative approach is to discover new systems that are potential hosts for strongly interacting phenomena. Discovering new quantum systems can be laborious and expensive; however, the dispersion of electrons can accurately be mimicked by classical waves, such as sound. The ability to quickly and cheaply 3D print acoustic metamaterials allows for rapid iterations and the discovery of novel lattice geometries which can then be brought to the quantum regime. I will present

the experimental measurement and simulation of macro-scale acoustic metamaterials to prototype new flat band lattices. Additionally, I will discuss the development of a novel platform for designing arbitrary dispersions of surface acoustic waves in piezoelectric crystals using metamaterials.

Contents

Citations to previously published work

Chapter 2 appears in its entirety as

[1] Benjamin H. November, Jay D. Sau, James R. Williams, Jennifer E. Hoffman, "Scheme for Majorana Manipulation Using Magnetic Force Microscopy," arXiv:1905.09792 (2019).

Chapter 5 appears in its entirety as

[2] Jeffrey Shi, Benjamin H. November, Stephen Carr, Harris Pirie, Jennifer E. Hoffman, "Quantum-inspired design of a tunable broadband high-Q acoustic resonator," arXiv 2412.20274 (2024).

Acknowledgments

Getting a PhD was one of the most exciting and challenging experiences on my life; and I wouldn't trade the past seven years for anything. The human connections I've made, from professional relationships to the deepest friendships I've yet known, I will carry with me for the rest of my life. And I have many people to thank for this wonderful adventure.

First and foremost, I have to thank my family for all of their love, support and encouragement during this long process. My parents supported me and my decisions to pursue knowledge at my own pace and in my own way, for which I am very grateful. My sister, Rachel, has been my rock and the foundation I've stood on, carrying the weight of not just her problems, but of mine as well, so that I could focus and finish this journey.

The single greatest strength I gained during my time at Harvard were the friendships I was lucky enough to develop along the way. To my best friends and roommates, Colby Banbury, Jon Alvarez, Ben Sibson, and Bhaven Patel, thank you for always being there and being my home, especially through the otherwise dark times of the pandemic. I also want to thank the members of "Rocket Power", an amazing group of friends and fellow PhD students, and especially Eliot Fenton and Josh Price, who helped get me through the highs and lows of the PhD. I'm also grateful to Andrés Mier-

Valdivia and Nathan Drucker for being not only great friends, but also great scientists, supporting me inside and outside of the lab.

The Hoffman lab was filled with amazing people who made doing research fun, even when it wasn't. Thank you to everyone for making the lab such a fantastic working environment. In particular, thank you to Harry Pirie for being an unbelievable mentor, role model, and advocate when I needed it. Thank you to Jacky Ge, Richard Liu, Mengke Liu, Christian Matt, and Tatiana Webb for being the guiding forces for the newest members of the lab and passing on the torch of STM knowledge we needed to excel. I'm also so thankful to all of the members, past and present, of the Nautilus STM team: Dilek Yildiz and Stefan Ulrich, for being there from the versy start of the project and helping see it through to the end; Gal Tuvia and Henry Bowman, for being eager learners and significant contributors even at some of our lowest moments; and a special thank you to Aaron Coe, without whom this project would not have been possible, you were a great partner and friend. I'm also grateful for my fellow graduate students and colleagues in the lab who were always available to lend a hand, a tool, or an ear: Ruizhe Kang, Kevin Hauser, Larissa Little, Tan Dao, and Anjola Bamtefa. I've also benefited greatly from Jason Hoffman, who provided feedback on pretty much every chapter of this thesis at one point or another, thank you.

I was lucky enough to work with some of the brightest young scientists Harvard has to offer over the course of my PhD, many of whom made this thesis possible. Im grateful to every single one of them. A special thank you is in order for Federico Maccagno, who took on several graduate student level projects and conquered them through hard work, dedication, and natural brilliance; for Jeffrey Shi, who I had the pleasure of working with since he was in high school, and I was able to see flourish into a brilliant young researcher; and for Yiting Huang, who has never known the word "quit", and I am very proud is continuing his scientific journey in graduate school. I'm thankful to Jasleen Kaur, Daria-Teodora Harabor, Rares-Georgian Mihalcea, Layan Ansari, and Daniel Shen for making the surface acoustic wave metamaterials project such a success. On the macroscopic acous-

tics side, I want to thank Walker Gillett, Radu Andrei, Fiona Abney-McPeek and Adrienne Chan for their efforts in simulating acoustic metamaterials using COMSOL, and Jiatong Yang, Bradley Baltz and Meghan Marangola for their hard work making the experimental realization of acoustic metamaterials a reality.

I had the great fortune of collaborating with some of the world's greatest minds during my time at Harvard. In particular, thank you to Jay Sau for his guidance and patience in developing the simulations that went into the second chapter of this thesis. I'm also thankful to Stephen Carr, who always provided the insight we needed whenever we hit a wall on a metamaterials project.
I truly believe a big part of what makes the Physics department at Harvard one of the best in the world is the staff, both administrative and maintenance. Although it is not specifically highlighted in this thesis, a huge amount of time and effort of my PhD went into the construction of a dilution refrigerator SPM, which would not have been possible without the help of Connie and Sean Concannon and Bobby Kinney. Additionally, thank you to Jacob Barandes and Lisa Cacciabaudo, who always had an open door when I had a problem or just needed guidance. The department wouldn't be what it is without them. Thank you to Silke Exner, Adam Ackerman, Helen Abraha, Dionne Clarke, and Erica Mantone for making the complications of scientific purchasing easier to manage.

Finally, I want to thank my thesis committee, Philip Kim and Ashvin Vishwanath, for their advice and guidance throughout the course of my PhD. And of course, thank you to my academic and research advisor Jennifer Hoffman, for all of her guidance and support throughout this long journey. I benefited immensely from having an advisor who believed in me, even when I may not have believed in myself. I have become a much better writer, thinker, and overall person from working with her, and for that I will always be thankful.

At last, I am grateful for the funding that made this work possible. The theoretical development of a protocol for Majorana manipulation was funded by the National Science Foundation QII-TAQS program, grant OMA-1936246. The construction of a milliKelvin microscope capable of carrying out this protocol was funded by the Gordon & Betty Moore Foundation, grant GBMF10215. The development of acoustic metamaterials to mimic and prototype quantum materials was funded by the Center for Integrated Quantum Materials (CIQM), NSF Science & Technology Center, DMR-1231319.

Part I

A new path towards topological quantum computing

1

The difficulty in achieving quantum computing

The last half century has seen an incredible exponential expansion in classical computing power as the size and cost of producing classical bits in the form of transistors has plummeted. However, there are certain problems for which classical computers still cannot easily solve. Examples date back as far as Richard Feynman's ideas of simulating large-scale quantum systems [3], a task exceptionally

hard for fundamentally classical objects. Another primary example of this is the factoring of large numbers into their composite primes, which in some ways has become the basis of many forms of modern encryption. This problem requires an exponentially larger number of computation steps as the size of the number to be factored grows, requiring *classical* compute power that is currently impossible. However, Peter Shor famously showed in 1997 that a *quantum* computer can complete this task in polynomial time [4]! Quantum computers take advantage of quantum entanglement, which means the number of possible states (called the Hilbert space) grows as $O(2^N)$, unlocking some problems previously inaccessible for classical computers. Such great promises have driven an enormous amount of effort over the past 40 years to achieve a scalable, reliable quantum computer, leading to the emergence of several different potential platforms, all with distinct advantages and disadvantages.

Fundamentally, most leading platforms for achieving scalable quantum computing rely on a two-level system to store information, in analogy to the CMOS transistor in modern classical electronics, called the qubit. These two-level systems have some ground state, $|0\rangle$ with a finite energy (or frequency since in quantum mechanics they are related by $E = \hbar\omega$) separation to a single excited state, $|1\rangle$, which is different from other energy gaps of nearby states. In classical computers, all the individual bits are encoded and act as separate two-level systems, but in a quantum computer all the individual two-level systems interact, and therefore transition between $|0\rangle$ and $|1\rangle$ in a correlated way, i.e. when measuring the state of a large number of qubits the probabilities to be in $|0\rangle$ or $|1\rangle$ should transition with the same frequency and phase [5]. In an ideal world, a quantum computer is a large set of individual qubits, coherently entangled and perfectly isolated from the rest of the world except during measurement or purposeful state changes by the user. In this case, even averaging over many trials over a large ensemble of qubits would always give the same result. However, in reality, interactions with the environment cause changes in the phase (amplitude) of these oscillations, leading to decoherence of the quantum state of the ensemble on average on a characteristic timescale, T_2

(T_1). Additionally, small changes in the frequency of the oscillations can also lead to decoherence over the course of many trial averages, which occurs on a generally shorter timescale T_2^*. This leads to the need for error correction schemes to fix flips in the qubit states to keep the overall decoherence low, or fault-tolerant. There has been much work to quantify the strict physical requirements complex error-correction algorithms must achieve [6, 7], but it remains an open challenge to make a quantum computer both fault-tolerant and scalable.

The primary obstacle to achieving scalable quantum computation is the vulnerability of qubits to environmental perturbation. To this end, there has been a strong push for the investigation of topological quantum computation (TQC) where protection from local fluctuations derives from the non-local nature of the qubit states, which greatly increases their stability [8]. Majoranas – emergent excitations that satisfy non-abelian exchange statistics – have been suggested as a key to TQC [9]. However, success of this approach requires a method to store and read out the information in the parity of a pair of Majoranas after an exchange. When two Majoranas are contracted to a single point, they can either annihilate or form a canonical fermion [10, 11]. The quantum information stored in the pair is the presence or absence of the charged fermion, so measurement of the increased charge or current density would constitute a readout of the parity of the Majorana pair. It is thus possible to use the braiding statistics and non-locality of Majorana states to create perturbation-resistant qubits.

Theoretical proposals involving Majoranas for quantum computation have existed for a quarter century, but the extreme challenges of experimental realization make the timescale for influence extremely long. The origin of this field is widely attributed to predictions by Read and Green [12] in 2000 and Kitaev [8] in 2003 that the low energy excitation spectrum of a spinless $p + ip$ superconductor would include a zero-energy solution with non-abelian braiding statistics. These predictions were followed by proposals to identify these zero-energy states in several systems, including vortices in $SrTiO_3$ [13] and excitations of the $\nu = 5/2$ fractional quantum Hall insulators [14, 15], which

sparked interest in the superconductor-semiconductor nanowire heterostructures. In the past few years, there have been numerous theoretical proposals for methods to braid and measure the parity of MZMs [16, 17, 18, 19, 20], but none have been realized.

The following chapter appears as:

arXiv:1905.09792 (2019)

B. H. November, et al.

2

A proposal for realizing topological quantum logic operations

Previous Majorana manipulation experiments have focused primarily on engineered heterostructures. For example, Majoranas at the ends of semiconductor nanowires on a superconducting substrate [21, 22] have shown some hard-won progress; however, due to tight constraints on temperature, magnetic field, and interface quality [23], experimental confirmation of recent theo-

retical proposals for Majorana braiding and qubit readout in nanowires [16, 17, 18, 19, 20] remains challenging. Another heterostructure approach involves superconductor/topological insulator/superconductor junctions, where Majoranas may be braided by Josephson vortex manipulation [24, 25], but experiments remain hampered by disorder and geometric constraints [26, 27]. Majoranas may also be found, in single clean materials where bulk *s*-wave superconductivity can self-proximitize the helical surface states of a topological semimetal or insulator, creating an effective topological superconductor on the surface [28]. Abrikosov vortex cores in these systems are predicted to host zero energy bound states with Majorana exchange statistics, known as Majorana zero modes (MZMs) [12, 29, 30]. Scanning tunneling microscopy (STM) experiments have observed zero bias conductance peaks (ZBCPs) suggestive of MZMs in the vortex cores of several Fe-based superconductors, including $FeTe_{0.55}Se_{0.45}$ [31, 32, 33, 34], $(Li_{0.84}Fe_{0.16})OHFeSe$ [35], $CaKFe_4As_4$ [36], and LiFeAs [37].

2.1 $FeTe_{0.55}Se_{0.45}$ as a platform for TQC

Vortices in conventional superconductors host Caroli-de Gennes-Matricon (CdGM) subgap states, which scale as $\pm\mu\Delta^2/E_F$, where Δ is the superconducting gap, E_F is the chemical potential [38], and μ is a half-integer. In topological superconductors, μ shifts to take on integer values, giving rise to a mid-gap zero energy state [39, 40]. $FeTe_{0.55}Se_{0.45}$ is among the primary candidates to utilize MZMs due to its relatively large $\Delta = 1.8$ meV and small $E_F = 4.4$ meV with respect to the Dirac point [31], yielding a sufficiently large spectral gap between CdGM states, such that an isolated ZBCP within can be easily distinguished by STM measurements at dilution fridge temperatures (Section I in [41]). $FeTe_{0.55}Se_{0.45}$ can thus host topologically protected qubits, but a scheme for the readout and manipulation of these qubits is still lacking.

Here we develop a general scheme for braiding MZMs in topological superconductors with vor-

tex manipulation and parity readout via magnetic force microscopy (MFM). We propose to first detect the MZMs in vortex cores by tunneling measurement of the ZBCP, then manipulate the vortices by magnetic force coupling from the MFM tip. While vortices have been shown to couple to locally applied mechanical [42], thermal [43], magnetic SQUID [44], and MFM [45, 46] probes, the higher spatial resolution of combined STM/MFM allows for sequential MZM identification in tunneling range, then magnetic manipulation and readout of MZMs at larger tip-sample separation to avoid quasiparticle poisoning. We quantify the feasibility of this general procedure to detect the Majorana pair parity for the specific material $FeTe_{0.55}Se_{0.45}$. By repeated measurements, the Majorana parity lifetime can be quantified, and ultimately more complex braiding could be used to conduct logical operations [47].

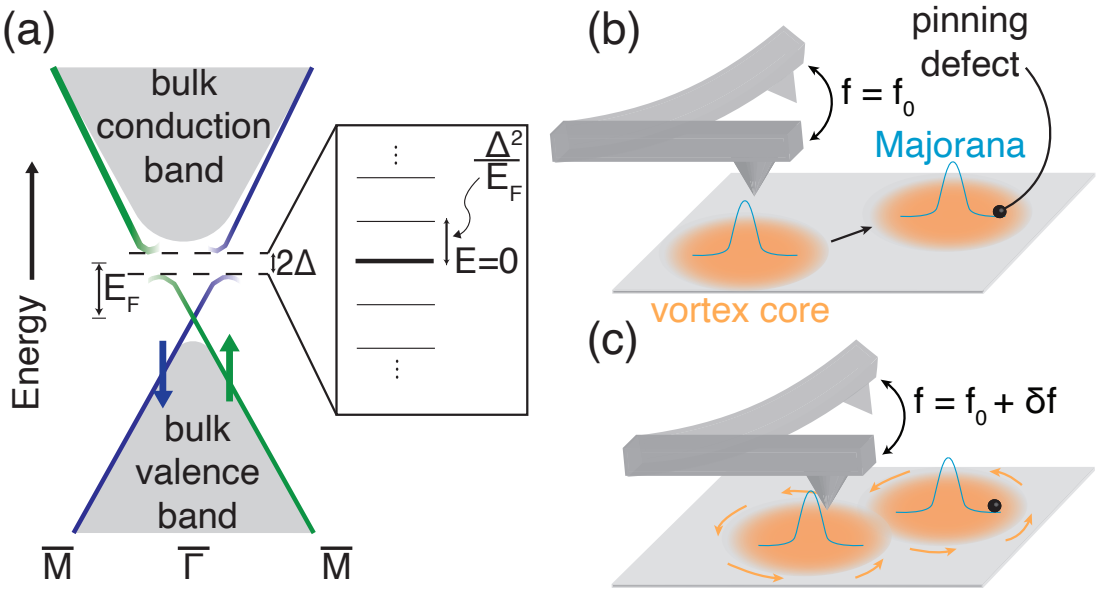

Figure 2.1: (a) Surface band structure schematic for Fe(Te,Se), supported by ARPES [48]. Inset shows the ladder of subgap states with a true zero mode (thick line) and trivial CdGM modes (thin lines) separated by Δ^2/E_F [38]. (b-c) Schematic of Majorana parity readout process. (b) MFM cantilever tip is used to bring one vortex close to another pinned vortex, causing the MZMs to overlap. (c) When in the parity 1 state, as shown here, the MZMs form a canonical fermion, generating an excess current density (orange arrows), and a corresponding change in cantilever resonance frequency δf, above the background (parity 0 state).

$FeTe_{0.55}Se_{0.45}$ exhibits bulk *s*-wave superconductivity up to $T_c = 14.5$ K [49, 50]. ARPES studies also find a surface Dirac cone [48], emerging from bulk inversion between an odd-parity *p* band and an even-parity *d* band along the Γ-Z direction [51], as illustrated in Fig. 2.1 a). Cooper pairs are free to tunnel between any of the pockets in the Brillouin zone and the surface states, leading to an effective internal proximity effect between bulk and surface. Therefore, $FeTe_{0.55}Se_{0.45}$ realizes the Fu-Kane model for proximity-induced *s*-wave superconductivity on topologically protected surface states [28].

We seek a measurement protocol for the quantum state of a pair of MZMs in two distinct vortices. Each Majorana operator $\gamma_{j=1,2}$ associated with these MZMs can be considered half a fermionic operator such that the combination $c^\dagger = \gamma_1 + i\gamma_2$ is a canonical fermion creation operator [10, 11]. The MZMs are fused by bringing the pair of vortices together to within a superconducting coherence length so their cores overlap, as depicted in Fig. 2.1 b,c). The occupation $c^\dagger c$ of the overlapping MZM pair then determines the presence or absence of an excess fermion, which would give rise to an excess charge and current density above the background of the fused vortices.

2.2 Double vortex parity signal

Parity readout—First, we will consider the limit where a pair of vortices are brought to completely overlap so that they fuse into a double flux quantum vortex. In this limit, polar symmetry reduces the problem to solving for the low energy eigenstates of the 1-D radial Bogoliubov-de Gennes (BdG) equation. Second, we will inspect the case of two spatially-separated single flux quantum vortices by discretizing the surface Hamiltonian and solving the BdG equation on a grid. We refer to these methods for solving the BdG equation as the continuum and lattice models, respectively. We can check the discretization error of the lattice model through comparison to the continuum model in the double flux quantum vortex limit. In both models, the occupancy of the lowest energy solution

measures the quantum state of the composite fermion formed by the overlap of the MZM pair.

Continuum Model - Double Vortex—A vortex state can be described by the BdG Hamiltonian:

$$H = [v_F \sigma \cdot p - E_F]\tau_z + [\Delta(\mathbf{r})\tau_+ + h.c.], \tag{2.1}$$

where p is the momentum operator of the topologically-protected surface state, v_F is the Fermi velocity, E_F is the chemical potential, and τ and σ are the Pauli matrices in Nambu and spin space, respectively [28, 52]. In polar coordinates, the gap is taken to be of the conventional form $\Delta(r/\xi) = \Delta(r/\xi)e^{in\theta} = \Delta_0 \tanh(r/\xi)e^{in\theta}$, where ξ is the coherence length, Δ_0 is the magnitude of the superconducting gap, and n is the winding number of the vortex. The Hamiltonian becomes

$$\begin{aligned} H = &-i\hbar v_F \left[(\sigma_x \cos\theta + \sigma_y \sin\theta)\partial_r + \frac{1}{r}(\sigma_y \cos\theta - \sigma_x \sin\theta)\partial_\theta\right]\tau_z \\ &- E_F\tau_z + \Delta(r)\left[\cos(n\theta)\tau_x + \sin(n\theta)\tau_y\right]. \end{aligned} \tag{2.2}$$

Equation 2.2 commutes with the total angular momentum operator and can thus be simplified by the appropriate choice of unitary transformation to the radial BdG equation given by

$$\begin{aligned} \Big[&- i\hbar v_F \sigma_x \tau_z \partial_r - \tau_z\Big(E_F + \frac{\hbar v_F}{2r}\sigma_y(\sigma_z + n\tau_z - 2m)\Big) \\ &+ \Delta(r)\tau_x - E\Big]\Psi(r) = 0, \end{aligned} \tag{2.3}$$

where m is the angular momentum quantum number of the vortex. We choose to work in units where $\hbar = v_F = \Delta_0 = 1$, forcing $\xi = 1$ and $\Delta(r) = \tanh(r)$. By rotating $\sigma_x \to \sigma_y$ about the z axis,

the BdG equation becomes real and 1-D, given by

$$\Big[\partial_r - \Big(iE_F\sigma_y - \frac{1}{2r}(1+\sigma_z(n\tau_z - 2m))\Big) - \tanh(r)\tau_y\sigma_y - iE\sigma_y\tau_z\Big]\Psi(r) = 0. \tag{2.4}$$

We seek the lowest energy solution $\Psi(r)$, for $m = \frac{1}{2}$ where a zero-energy solution exists for a double flux quantum vortex ($n = 2$) (Sections II-III in [41]). Though the system was solved analytically in the chiral limit where $E_F = 0$ [53, 28], here we solve Eq. 2.4 for the more realistic condition $E_F/\Delta_0 = 2.5$, comparable to the measured value for $FeTe_{0.55}Se_{0.45}$ [31]. The occupation of the state $\Psi(r)$ is associated with excess charge and current density above the background of the double flux quantum vortex, shown in Fig. 2.2(a-b). The excess charge density will exert an electrostatic force on the MFM tip, but screening by the background superconductor is expected to reduce this force to an undetectable level at tip-sample separation outside the tunneling regime. Therefore, we focus on the excess current density associated with $\Psi(r)$, given by the expectation value of the tangential component of the current operator,

$$j(r) = -v_F e\Psi^\dagger(r)\sigma_x\Psi(r). \tag{2.5}$$

For Majorana parity readout, the magnetic field gradient generated by this current $|dB_z/dz|$, shown in Fig. 2.2(c), must be detectable by MFM at tip-sample separations $\gtrsim$ 2 nm, where quasiparticle poisoning from tip-sample tunneling is not significant [13, 54, 55].

2.3 Spatially separated vortices

Lattice Model - Two Vortices—Experimentally, it may be difficult to sustain a true double vortex for a prolonged period. It's then critical to analyze the magnetic signal generated by the more realistic

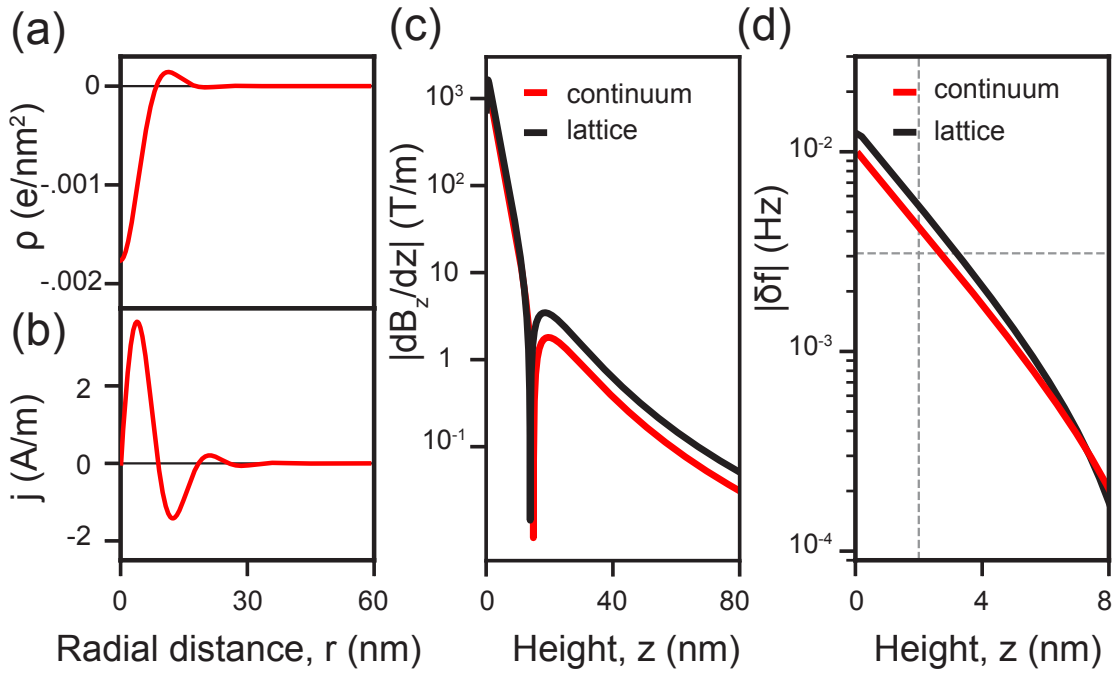

Figure 2.2: Calculated parity 1 signal. (a) Excess surface charge and (b) surface current density associated with the lowest energy wavefunction of a double flux quantum vortex as a function of lateral distance r from the vortex center. Calculations performed using the continuum model with $E_F/\Delta = 2.5$, comparable to the measured value for $FeTe_{0.55}Se_{0.45}$ [31]. (c) Excess magnetic field gradient $|dB_z/dz|$ as a function of height z above the center of a double flux quantum vortex in the parity 1 state, in the continuum (red) and lattice (black) models. (d) Resulting shift in MFM cantilever resonance frequency $|\delta f|$, calculated using Eq. 2.6 for the soft cantilever in Table S2 (row 2) with the Fe-coated nanowire tip in Table S3 (row 1) [41]. Specifically, we model a horizontal cantilever with $k = 0.006$ N/m, $f_0 = 13$ kHz, and $Q = 5 \times 10^4$, with a magnetic nanowire tip of effective monopole $\widetilde{m} = 0.04$ nA·m, offset by $d = 4.6$ nm from the nanowire apex. The low-temperature noise floor for this cantilever (horizontal gray dashed line) is calculated via Eq. 2.7 (Section V in [41]). Quasiparticle poisoning is expected to be negligible at tip heights $\gtrsim 2$ nm (vertical gray dashed line).

case of two partially-overlapping single flux quantum vortices, which we achieve by numerically solving the Fu-Kane Hamiltonian (Eq. 2.1) on a lattice. This discretized realization breaks time-reversal symmetry on the lattice level (as expected from the fermion doubling theorem), but is parameterized to preserve the low-energy effective Hamiltonian consistent with Eq. 2.1 (Section IV in [41]). The result of the lattice model in the extreme limit of the double flux quantum vortex is

shown in Fig. 2.2(c), demonstrating excellent agreement with the continuum model.

The Majorana signature can now also be studied as a function of the spatial separation of vortices. The current flow generated by the overlap of the two MZMs in the parity 1 state is shown in Fig. 2.3(a-d) for several spatial separations (the parity 0 case would have no such excess supercurrent). We calculate the excess field gradient $|dB_z/dz|$ at a fixed height $z = 2$ nm above the surface, as a function of the lateral separation between vortices, as shown in Fig. 2.3(e). The Majorana parity 1 signal decays exponentially with vortex separation as expected.

2.4 MFM Sensitivity and Noise

When the MFM tip approaches the vortex from above, the tip feels a force due to the magnetic field induced by the current density. The cantilever frequency shifts in proportion to the magnetic field gradient with sensitivity

$$\delta f = \widetilde{m}\frac{f_0}{2k}\frac{dB_z}{dz}, \tag{2.6}$$

where k is the cantilever force constant and f_0 is the cantilever resonance frequency (Table S2 in [41]), and $\widetilde{m}$ is an effective magnetic monopole, located a distance d within the tip apex (Fig. S1a in [41]). Here δf depends on dB_z/dz evaluated at the effective monopole location, i.e., the tip-sample separation z plus the internal distance d. For a typical commercially-available magnetically-coated pyramidal tip, $\widetilde{m} \sim 18$ nA·m (approximately 5 times the hypothetical fundamental Dirac monopole $h/e\mu_0$), but $d \sim 250$ nm [45], a large distance that reduces the overall frequency shift. To maximize the measurement sensitivity, it is optimal to use a magnetically coated nanowire on tip [56]. For example, an Fe nanowire with radius $r_{\text{wire}} = 6$ nm has a much smaller offset $d = 4.6$ nm, which outweighs the disadvantage of a smaller monopole $\widetilde{m} = 0.04$ nA·m (Table S3 in [41]).

The MFM *sensitivity* must be balanced against the three primary *noise* sources in frequency-

modulated AFM: thermal, detector, and oscillator noise [57, 58] (Section V in [41]). With optimized electronics and a typical silicon cantilever, even at low temperature the system will usually be dominated by thermal noise,

$$\delta f_{\text{therm}} = \sqrt{\frac{k_B T B f_0}{\pi k Q A^2}}, \tag{2.7}$$

where B is the measurement bandwidth, A is the oscillation amplitude, Q is the cantilever quality factor, and k_B is Boltzmann's constant. Then a stiffer cantilever lowers the noise floor as $\sqrt{f_0/k}$ according to Eq. 2.7, but also reduces signal sensitivity as f_0/k according to Eq. 2.6, making softer cantilevers the optimal choice for a parity readout. We modeled a commercially-available soft horizontal cantilever with $f_0 = 13$ kHz, $k = 0.006$ N/m, and $Q = 50,000$, and an Fe nanowire tip, to convert the vertical magnetic field gradient to a detectable frequency shift in Fig. 2.2(d) and Fig. 2.3(f). The corresponding noise floor for this cantilever, calculated in a 5 Hz bandwidth with a 2 nm oscillation amplitude, is drawn as a horizontal dashed line. Figure 2.2(d) shows that for a double flux quantum vortex, the calculated $|\delta f|$ from the parity 1 state does not drop below the noise floor until $z > 3$ nm, well out of the tunneling regime, making it possible to detect the parity 1 signal without poisoning the MZM. Fig. 2.3(f) shows that the parity 1 state $|\delta f|$ remains above the noise floor even for vortex separations up to 20 nm, larger than the coherence length in $FeTe_{0.55}Se_{0.45}$ [31]. Other background frequency shifts from the conventional vortex supercurrent and tip stray magnetic field are constant across all vortices (Section VI in [41]).

To read Majorana parity, we will need to bring two vortices together so their cores almost touch, overcoming the inter-vortex repulsion. In $FeTe_{0.55}Se_{0.45}$, which is at the extreme type-II limit, the vortex-vortex repulsion approaches 10 pN for a 100 nm thick film as the separation approaches 2ξ [59] (Section VII in [41]). Therefore, we must strongly pin one vortex in a region where topological band inversion guarantees a surface MZM [60], while we bring another vortex towards it. Assuming a typical 100 nm $\times$ 100 nm scan frame, this corresponds to a desired approximate applied perpen-

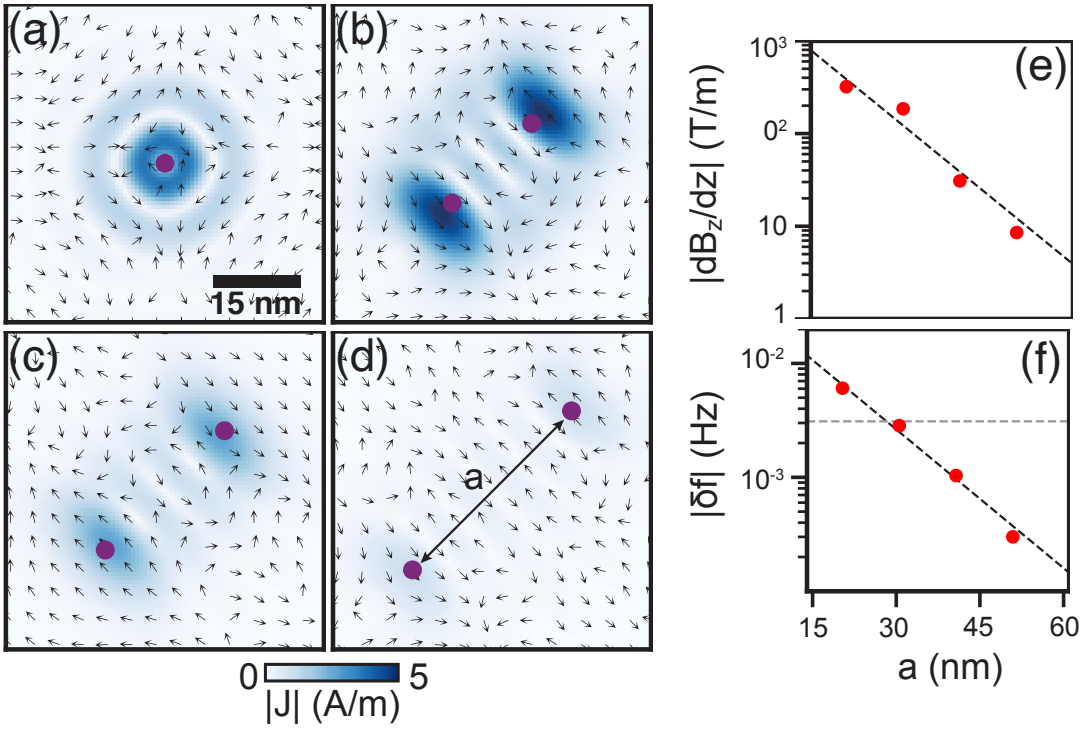

Figure 2.3: Excess current density generated by overlap of two MZMs in the parity 1 state in the lattice model with $E_F/\Delta = 2.5$ for (a) the double flux quantum vortex and vortex cores (purple dots) separated by (b) $a \sim 2\xi$, (c) $a \sim 2.5\xi$, and (d) $a \sim 3.5\xi$. (e) Excess magnetic field gradient $|dB_z/dz|$ caused by the parity 1 state as a function of vortex separation a. Evaluation point is 2 nm above the midpoint between the two vortex cores. Black dashed line is an exponential fit showing the decay as a function of vortex separation. (f) Resulting shift in MFM cantilever resonance frequency $|\delta f|$, calculated using Eq. 2.6 for the soft cantilever in Table S2 (row 2) with the Fe-coated nanowire tip in Table S3 (row 1) [41]. Gray dashed line shows the low-temperature noise floor for this cantilever, calculated via Eq. 2.7 (Section V in [41]).

dicular external magnetic field of $B_\perp^{\text{ideal}} \approx 2\Phi_0/(10^{-7})^2 = 414$ mT. Though pinning forces in clean bulk FeSe can be on the order of fN [61], a promising measurement in ion-irradiated $FeTe_{0.55}Se_{0.45}$ showed that some vortices can be fixed by collective pinning in relatively clean areas [62], avoiding MZM burial or poisoning by normal quasiparticles present at the pinning site, and leaving a sharp ZBCP intact on the surface.

2.5 Parity Lifetime Measurement

Despite its topological nature, the Majorana pair has a finite parity lifetime due to interactions between Majoranas and stray quasiparticles that cause decoherence known as quasiparticle poisoning [63]. Quasiparticle poisoning leads to a fluctuation of the occupation of the lowest-energy vortex bound state, and thus the excess magnetic field that we propose as a parity readout signal. These discrete flips in the Majorana parity between 0 and 1 would give rise to telegraph noise in the force on the MFM tip as it is held above the vortex cores, providing insight into the Majorana poisoning time. While for a uniform, closed system, the quasiparticle poisoning time is exponentially suppressed by the Boltzmann factor $e^{-\Delta/k_B T}$ [64], disorder and spurious microwave sources can increase the density of quasiparticles and thus the frequency of parity flips. In addition, the presence of this telegraph noise could also serve as a high-frequency signal to help quantify and subtract the vortex background [18] (see Section VI in [41]). A recent demonstration of Majorana parity readout in an InAs-Al hybrid device [**?**] exhibited a telegraph noise on the order of 2 ms. The strong spin-orbit coupling of an intrinsic topological superconductor such as $FeTe_{0.55}Se_{0.45}$ permits weaker applied magnetic fields compared to the few Tesla magnetic field required to open the topological gap in semiconductor-superconductor hybrid devices, potentially opening the door for a larger topological gap and correspondingly longer poisoning times $\geq$ 10 ms.

Majorana telegraph noise should be measurable if the quasiparticle poisoning is slower than the acquisition of the force measurement. The characteristic rate of telegraph noise would yield an estimate of the quasiparticle poisoning timescale that limits the qubit lifetime, which has been difficult to model and is poorly understood. To minimize extrinsic quasiparticle poisoning, the tip must be out of tunneling range, $z \gtrsim 2$ nm from the surface. From Fig. 2.2(d), this z corresponds to an expected signal $\delta f \sim 5$ mHz, which requires a measurement time ~ 200 s in frequency-modulated MFM. However, using amplitude-modulated MFM, the measurement duration is limited only by

the response time of the cantilever to a changing force. In ultra high vacuum, Si cantilevers can have $Q \sim 50,000$, but lossy cantilevers with $Q \sim 100$ and $f_0 \sim 10$ kHz could enable much faster measurement $Q/f_0 \sim 10$ ms. Q can also be tuned in situ for a given cantilever by a factor of 20 or more [65].

Conclusion—We have presented a general scheme for the pinning, dragging, parity readout, and lifetime measurement of a pair of MZMs in the vortex cores of topological superconductors using MFM. We have shown that MFM cantilevers can be sensitive enough to measure the change in supercurrent when the resulting fermionic state is occupied, even when the two vortex cores are not completely overlapping. While we have explicitly demonstrated numerical feasibility only for $FeTe_{0.55}Se_{0.45}$, we expect the same methodology will be applicable to other topological superconductors that realize the Fu-Kane model on the surface, including stoichiometric materials with uniform chemical potential (Table S1 in [41]). Thus, we have laid out a novel pathway toward the experimental realization of topologically protected quantum logic.

Part II

Acoustic metamaterials as a platform for quantum material exploration

3

A coupled resonator by any other name

3.1 Quantum-classical analogy

The physics community has invested an enormous amount of time and effort in convincing ourselves and the world that when objects become "small" enough (relative to Planck's constant $\hbar$), the set of fundamental laws governing their behavior change. The familiar expressions from classical mechanics of position and velocity are no longer deterministic, but probabilistic. The same quan-

tum mechanical principles apply to more than just one individual particle, to collections of many particles closely packed together. Condensed matter systems are then a natural testbed for predictions of quantum mechanics, such as the specific heat and electrical conductivity of materials as a function of temperature.

However, not all of the behavior of electrons in quantum materials are exclusive to the quantum realm. In fact, classical waves, such as sound, can reproduce much of the dispersion behavior as electrons in a solid. At first glance, this seems counter-intuitive, after all, the underlying mechanical equations of the two systems are different. Electrons are governed by the time-dependent Schrödinger equation, which is usually written in the form:

$$-i\hbar\frac{\partial}{\partial t}\left|\psi(x,t)\right\rangle = \hat{\mathcal{H}}\left|\psi(x,t)\right\rangle \tag{3.1}$$

where $|\psi(x,t)\rangle$ is the many-body wavefunction containing all the information about the quantum state of the system, and $\hat{\mathcal{H}}$ is the Hamiltonian operator describing how the system evolves in time. In general, with interaction terms in the Hamiltonian, the number of terms in the Schrödinger grows exponentially large with the number of particles in the system, making it impossible to solve exactly. However, under some simplifying conditions the above equation can be made to look quite familiar. In free space for non-interacting electrons, the Hamiltonian is only the kinetic energy operator $\frac{\hat{p}^2}{2m}$ where $\hat{p}$ is the momentum operator and m is the bare mass of the electron. In 1D, the momentum operator in real space is given by $\hat{p} = i\hbar\frac{\partial}{\partial x}$, so the Schrödinger equation simplifies to

$$i\hbar\frac{\partial}{\partial t}\left|\psi(x,t)\right\rangle = \frac{\hbar^2}{2m}\frac{\partial^2}{\partial x^2}\left|\psi(x,t)\right\rangle . \tag{3.2}$$

If we assume a plane wave solution for the wavefunction, i.e. a solution of the form $|\psi(x,t)\rangle = Ae^{-i\omega t}(e^{-ip\cdot x/\hbar} + e^{ip\cdot x/\hbar})$, we recover the dispersion relation for electrons in free space:

$$\hbar\omega \, |\psi(x,t)\rangle = \frac{p^2}{2m} \, |\psi(x,t)\rangle \tag{3.3}$$

$$\hbar\omega = \frac{\hbar^2 k^2}{2m} \tag{3.4}$$

$$\implies \omega \propto k^2 \tag{3.5}$$

where $k = p/\hbar$ is the wavenumber. The relationship between the temporal frequency, ω, and the wavenumber, (or you can think of it as the spatial periodicity) k, is called the *dispersion relation* for the free electron. The key feature here is that ω scales as k^2. This is in contrast to classical waves that obey the wave equation, such as longitudinal sound waves, where $\omega \propto k$. We can see this from the form of the acoustic wave equation

$$B(\vec{x})\nabla \cdot \frac{1}{\rho(\vec{x})}\nabla P(\vec{x},t) = \frac{\partial^2}{\partial t^2} P(\vec{x},t) \tag{3.6}$$

where $B(\vec{x})$ is the bulk modulus and $\rho(\vec{x})$ is the density of the medium. Assuming a uniform material in 1D this reduces to

$$\frac{B}{\rho}\frac{\partial^2}{\partial x^2} P(x,t) = \frac{\partial^2}{\partial t^2} P(x,t), \tag{3.7}$$

$$\tag{3.8}$$

which is exactly the form of the wave equation $\frac{\partial^2}{\partial t^2}\psi(x,t) = c^2 \frac{\partial^2}{\partial x^2}\psi(x,t)$ with $c = B/\rho$ the speed of sound. The wave equation gives rise to a linear dispersion relation, $\omega \propto k$, unlike the quadratic dispersion for the quantum equivalent. How then can sound reproduce electronic dispersion relations in in condensed matter systems? The answer lies in the fact that we are not concerned with

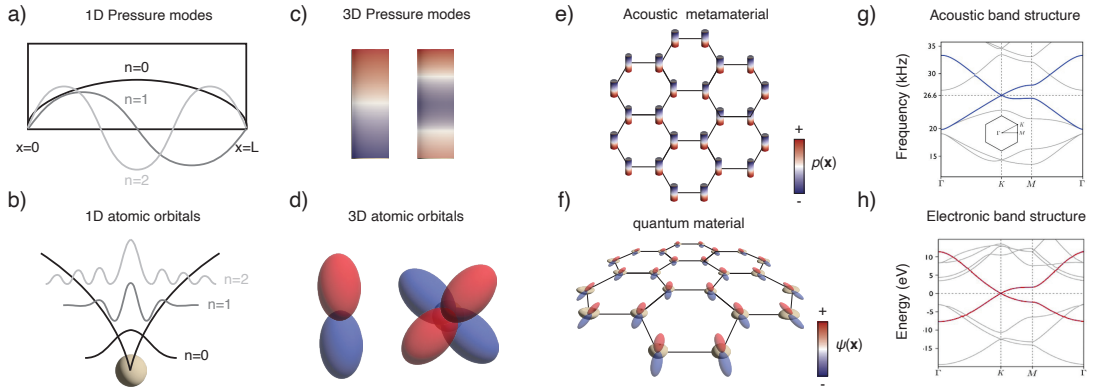

Figure 3.1: Acoustic metamaterials capture single-particle quantum physics. **a,** Sound waves in 1D trapped in a box of sound hard boundaries form a ladder of evenly spaced eigenstates. The lowest few generic eignestates are sketched in gray. **b,** electrons trapped in the coulomb potential well generated by a proton also form a ladder of bound states. Illustrations of the radial component of the lowest few levels are shown in gray. **c,** A 3D air cavity in a solid material will host resonance modes with symmetries relating to its container, in this case, a cylinder. Red and blue represent high and low acoustic pressure compared to atmosphere, respectively. **d,** The 3D solutions to the hydrogen atom form the basis of atomic orbitals we are familiar with, in this case an example p (left) and d (right) orbital. Red and blue represent positive and negative phase of the wavefunction. **e,** A honeycomb acoustic metamaterial is constructed from coupling many of the acoustic cavities such as those shown in **c,** through thin air channels. **f,** Graphene is a honeycomb lattice of carbon atoms connected by covalent bonds. **g,** The honeycomb acoustic metamaterial reproduces the expected band structure of graphene with the signature Dirac crossing at the K point. **h,** The electronic band structure of graphene calculated via tight-binding model.

replicating the behavior of non-interacting electrons in free space, but in crystals where electrons strongly feel the background lattice.

3.2 Acoustic metamaterials as quantum mimics

Instead of the free space picture, take instead the limit of electrons and sound waves trapped in a strong potential well. For sound, this is the solid walls of a container full of air, and for electrons, the coulomb potential from the positively charged nuclei of the crystal lattice. Consider a 1D box full of air of length L with sound hard boundaries on both sides. The displacement must go to zero at $x = 0$, fixing the solution for $\psi(x)$ to be a $\psi(x) = A\sin(kx - \omega t)$, and $x = L$, enforcing $k_n = n\pi/L$, and thus $\omega = ck_n = n\pi/L$ for a positive integer n. By restricting the sound waves

to a finite container, the solutions to the wave equation have become a ladder of states, analogous to the solutions for the hydrogen atom. Similarly, when many resonators are put together in a periodic array, whether they be tunneling electrons or connected air cavities, the emergent band structure of eigenstates is determined by the geometry of the lattice alone. Although the level spacing and exact functional forms of the wavefunctions depend on the natural constants and exact potential well functional forms in the problem, the emergent ladder solution allows direct comparisons to be drawn between the two systems!

In the following chapters, I will take advantage of this analogous behavior between classical resonators and tightly bound non-interacting electrons to explore the physics of 2D systems that have yet to be realized in the quantum setting. By simulating or building the acoustic lattice analog, called an acoustic metamaterial, we are able to understand the band structure of lattices that, until now, are poorly studied or in a physical regime otherwise not achievable in a controllable way in quantum materials. For example, stacked, twisted vdW systems have been of high interest in the condensed matter community since the discovery of superconductivity [66] and correlated insulator [67] states in magic angle twisted bilayer graphene (TBG). The emergence of these interesting states is mainly contributed to the flattening of the Dirac bands around the K point due to the moiré potential [68]. The surprising nature of this discovery has lead to much effort in understanding TBG, wich has come to be well modeled from the non-interacting band perspective. However, as more layers and different 2D layer constituents are added to heterostructures, they become very difficult to model. Metamaterials offer the advantage of not being limited to any particular set of constituent layers since the geometry is perfectly controllable. If a system is too large to simulate, by tight-binding, finite element, or any other methods, it can instead be 3D printed and measured. In this way I envision metamaterials as a rapid and cheap prototyping platform for discovering and understanding new quantum materials.

The following chapter appears as:

arXiv 2412.20274 (2024)

J. Shi, **B. H. November**, et al.

4

Acoustic harmonic oscillator

Acoustic metamaterials that adapt quantum concepts to the classical domain have led to applications such as topological insulator lasers [69, 70], acoustic logic gates [71, 72], and materials with zero or negative refractive index [73, 74, 75]. Here, we design a broadband high-Q acoustic resonator by mimicking the dense array of flat bands found in a wide range of twisted semiconductor heterostructures[76, 77, 78], including h-BN, $MoSe_2$, WSe_2, and WS_2 [79, 80, 81]. The relative twist between layers generates a long-range moiré pattern in these materials, resulting in a grad-

ual variation of their interlayer alignment and the creation of a smoothly varying potential, $V(\mathbf{r})$. This potential changes the local bilayer Hamiltonian while leaving each monolayer band structure mostly intact [68, 82, 83]. The flat bands of these twisted semiconductors thus have a straightforward explanation: the parabolic kinetic energy dispersion $E(\mathbf{k}) \propto |\mathbf{k}|^2$ of each monolayer band edge combines with the parabolic spatial potential of the moiré pattern $V(\mathbf{r}) \propto |\mathbf{r}|^2$ to give a textbook example of a harmonic oscillator [84, 85, 86], characterized by the local Hamiltonian

$$H = \frac{|\mathbf{p}|^2}{2m^*} + \frac{1}{2}m^*\omega_0^2|\mathbf{r}|^2, \tag{4.1}$$

where m^* is the effective electron mass and ω_0 is the oscillator's frequency. This ladder of harmonic oscillator states differs from the well-known pair of flat bands in magic-angle twisted bilayer graphene [66], which arises from the hybridization of Dirac cones at fixed energy.

4.1 Design of metamaterial

Here we design an acoustic metamaterial analog of twisted bilayer graphene where the harmonic oscillator flat bands manifest as multiple high-Q resonance modes with controllable frequency, number, and spacing. We start by designing two-dimensional acoustic metamaterials that mimic an electronic tight-binding model. Each lattice site consists of a cylindrical air hole (density 1.2 kg/m^3, speed of sound 343 m/s) in a steel sheet (density 7850 kg/m^3, speed of sound 5790 m/s), supporting single-cavity acoustic modes with frequency spacing set by the cavity size. We connect these modes through thin channels to allow nearest-neighbor intralayer hopping $t_{||}$, and focus on the lowest (s-band) manifold of states, whose dispersion closely mimics that of monolayer graphene [87]. To implement an interlayer coupling strength t_z, we insert a thin steel membrane between two vertically stacked graphene metamaterial layers [88]. The couplings $t_{||}$ and t_z are controlled by the channel width or interlayer membrane thickness, respectively. For a resonator in the audible range, we

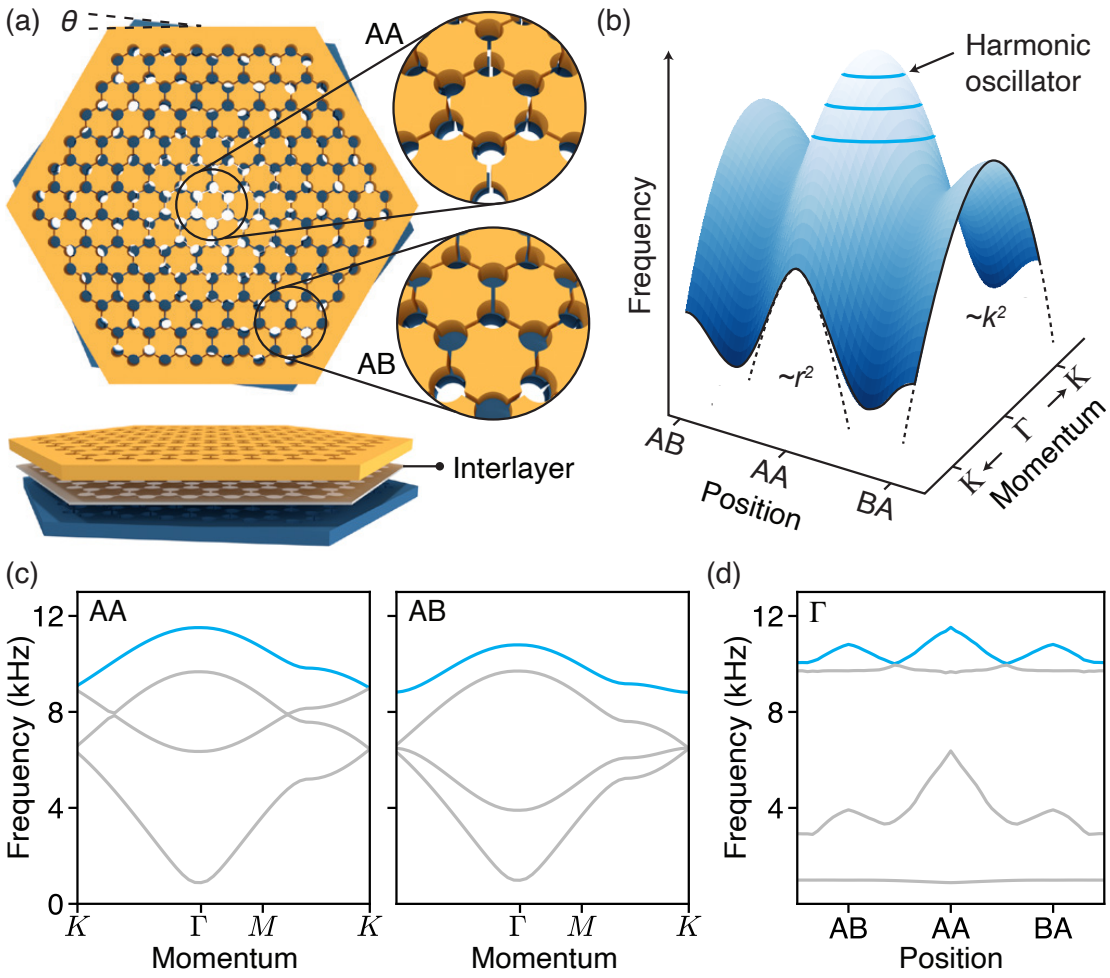

Figure 4.1: A moiré potential generates an effective harmonic ocsillator Hamiltonian. a, Acoustic metamaterial design to mimic twisted bilayer graphene. **b,** Schematic of the band energy as a function of $\mathbf{k}$ and $\mathbf{r}$. At both AA and AB stacking the local band energy can be approximated by a parabola, leading to harmonic oscillator states near the local maxima. **c,** Calculated band structures for symmetric stacking configurations of acoustic bilayer graphene. At the Γ-point, the top band of the *s*-manifold (blue) is well approximated by a parabolic dispersion with negative curvature. **d,** Γ-point band edge frequency as a function of stacking configuration, calculated from an untwisted bilayer metamaterial with a lateral translation between the layers. This real-space band dispersion constitutes an effective potential $V(\mathbf{r})$ for the acoustic waves, which is locally parabolic at AA and AB.

choose a cavity radius of $R = 3.25$ mm, nearest-neighbor spacing $a = 10$ mm, channel width $w = 0.875$ mm, metamaterial layer thickness $D = 1$ mm, and interlayer thickness $T = 25\,\mu$m. Finally, we introduce a twist angle $\theta = 3.89^\circ$ between the layers to generate an acoustic moiré super-

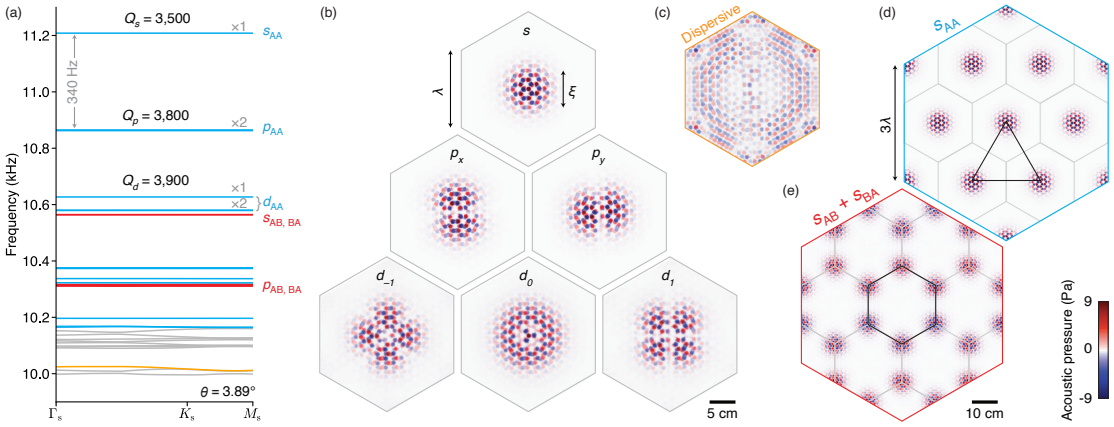

Figure 4.2: Harmonic oscillator potential generates a ladder of high-Q resonances. a, Acoustic band structure of a 3.89° twisted metamaterial at frequencies around the Γ-point band edge at the top of the s-manifold. The AA-localized flat bands (blue) are approximately equally-spaced with $\omega_0 \approx 340$ Hz. The flat bands are either one-fold ($\times 1$) or two-fold ($\times 2$) degenerate. Harmonic oscillator states also localize on the AB/BA symmetry regions (red). A representative dispersive band is highlighted in orange. The Q-factors are calculated by placing a monopole acoustic point source in one of the cavities in the central unit cell with a free space reference root mean square power of 0.01 W. Losses through air cavities are modeled under atmospheric attenuation at standard temperature (293 K) and pressure (1 atm) conditions. Losses in the steel are defined with an attenuation coefficient of $\alpha = 0.05$ dB/m. **b,** Pressure distribution of the AA-centered harmonic oscillator states labeled according to their angular harmonics. **c,** Real-space pressure distribution for the representative dispersive mode. **d-e,** Pressure distribution over several moiré periods, showing larger moiré crystals with an effective triangular (d) or honeycomb (e) lattice.

lattice analogous to twisted bilayer graphene, as shown in Fig. 4.1a. We calculate the pressure eigenmodes and band structure of this system using the Pressure Acoustics, Frequency Domain interface within the acoustic module of the commercial finite-element software COMSOL Multiphysics®. The three pairs of side boundaries of the moiré supercell are given periodic Floquet boundary conditions while the outer faces of the top and bottom steel sheets are impedance matched to air.

4.2 Origin of harmonic potential

Harmonic oscillator states form within a band dispersion that is locally parabolic in both real and momentum space (Fig. 4.1b), mimicking the behavior described by equation (4.1). The top band of the s-manifold of bilayer graphene has a kinetic energy dispersion $E(\mathbf{k}) \propto -|\mathbf{k}|^2$ around the Γ point,

as calculated in our honeycomb metamaterial (blue line in Fig. 4.1c). Across the moiré supercell, the interlayer coupling t_z is strongest when all the cavities perfectly overlap (AA stacking) and weakest when the overlap is smallest. This local variation in t_z creates a position-dependent potential, $V(\mathbf{r})$, which can be approximated for small θ by the stacking configuration of two untwisted layers with a relative shift[83], as shown in Fig. 4.1d. In our acoustic metamaterial, the Γ-point eigenfrequency of the upper band peaks at the AA, AB, and BA stacking configurations, corresponding to a local potential $V(\mathbf{r}) \propto -|\mathbf{r}|^2$ (blue line in Fig. 4.1d). We expect harmonic oscillator states to emerge within these local maxima because the **k**-space curvature of the Γ-point band dispersion has the same sign as the **r**-space moiré potential. This scenario leads to a local Hamiltonian equivalent to equation (4.1) with a negative effective mass. The angular frequency of the harmonic oscillator can be approximated by [84]

$$\omega_0 = \sqrt{\frac{\partial^2 H(\mathbf{k},\mathbf{r})}{\partial \mathbf{k}^2}\frac{\partial^2 H(\mathbf{k},\mathbf{r})}{\partial \mathbf{r}^2}}. \tag{4.2}$$

We estimate the **k** and **r** space curvatures by fitting parabolas to the blue band maxima in Fig. 4.1c and d, yielding an expected level spacing of $\omega_0 \approx 340$ Hz for the AA point from equation (4.2).

4.3 Emergent ladder of harmonic states

By twisting the metamaterial as illustrated in Fig. 4.1a, our simulation reveals a ladder of harmonic oscillator states localized around the AA sites, shown in Fig. 4.2a. These states form flat bands with roughly equal spacing $\omega_0 \approx 340$ Hz, in excellent agreement with the independent approximation from the shifted metamaterial using equation (4.2). The bands have extremely narrow intrinsic linewidths $\Delta f \sim 1\,\mu$Hz, corresponding to a quality factor $Q \equiv f/\Delta f$ exceeding 10^{10}. However,

when we account for realistic acoustic losses due to damping within air and steel, Q falls to around 4,000, which still exceeds typical measured Q for airborne acoustic devices at ambient conditions [89, 90]. By optimizing material selection, this design concept has the potential to achieve ultra-high Q.

In real space, the harmonic oscillator modes exhibit well-defined spatial symmetries, as shown in Fig. 4.2b. The spatial patterns are the angular harmonics of a two-dimensional quantum harmonic oscillator, and we label these modes as s, p, and d orbitals, in analogy to the orbital states of electrons around a nucleus. In contrast, dispersive bands with non-localized real-space distributions form below the potential well, shown in Fig. 4.2a,c. As expected, the s mode is non-degenerate, and the p mode is two-fold degenerate. Meanwhile, the d modes exhibit degeneracy breaking, with the d_0 mode splitting from the d_{-1} and d_1 modes, likely due to the anharmonicity of the moiré potential well. Moreover, these harmonic oscillator states couple to create larger spatial arrays of high-Q modes, forming an emergent triangular lattice on the moiré length scale (Fig. 4.2d).

Harmonic oscillator states also emerge at the AB and BA sites, where $V(\mathbf{r})$ has additional local maxima. In this case, only the s and p AB/BA harmonic modes fit within the potential, highlighted as red lines in Fig. 4.2a. The level spacing $\omega_0 \approx 250$ Hz is smaller than the AA-localized modes, reflecting the wider local curvature of the potential around AB/BA (see equation (4.2)). In contrast to the AA-localized modes, which form a triangular lattice with nearest-neighbor distance $\sqrt{3}\lambda$, the composite AB/BA-localized modes form a honeycomb lattice with nearest-neighbor distance λ.

In the stacked two-dimensional semiconductor systems that inspired this work [79, 80, 81], the moiré potential is determined by the microscopic interactions between electrons and atoms, limiting tunability. In contrast, the interlayer coupling in a metamaterial can be continuously tuned by adjusting the interlayer thickness [88]. A stronger interlayer coupling increases the Γ-point band splitting, which deepens the harmonic oscillator potential well V_0, as shown in Fig. 4.3a. A deepened well allows for an extended ladder of harmonic oscillator modes, enabling access to those with

higher angular momentum.

4.4 Tunability

Our metamaterial also allows the width of the potential well to be tuned. The potential $V(\mathbf{r})$ can be widened by decreasing the twist angle, which moves the AB points further away from the AA point, stretching the same change in t_z over a longer length scale. A wider $V(\mathbf{r})$ reduces the curvature $\partial^2 H(\mathbf{r})/\partial \mathbf{r}^2$, leading to more closely spaced resonances from equation (4.2). The relationship between level spacing and twist angle is nearly linear, suggesting that harmonic oscillator modes become densely packed in frequency as the twist angle approaches zero (Fig. 4.3b). For instance, adjusting the twist angle from 6° to 2° increases the number of non-degenerate harmonic oscillator modes from 4 to 25 (inset in Fig. 4.3b). At a twist angle of 2°, we found that although the s and p modes are separated by about 200 Hz, higher angular momentum modes can be spaced as little as 10 Hz apart. Crucially, this low-twist regime yields an acoustic resonator that maintains a high Q over a wide bandwidth (Fig. 4.3c,d), overcoming the typical trade-off between Q and bandwidth.

Acoustic twisted vdW metamaterials offer a promising platform for realizing broadband, high-Q resonance modes. Our twisted bilayer metamaterial reveals a ladder of harmonic oscillator modes localized around the AA, AB, and BA stacking configurations. The depth and width of the harmonic potential well depend on continuously tunable properties of the metamaterial, allowing the number and frequency separation of the resonances to be adjusted as desired. Unlike traditional acoustic fabrication techniques where binary potentials are encoded through sudden changes in material density, our approach inherits a smoother long-range potential from the moiré pattern. This smooth potential, combined with the strong localization and multi-cavity nature of these emergent modes, makes them resilient to local fabrication defects. We anticipate these resonators will advance applications requiring broadband, high-Q performance, such as efficient amplification for energy har-

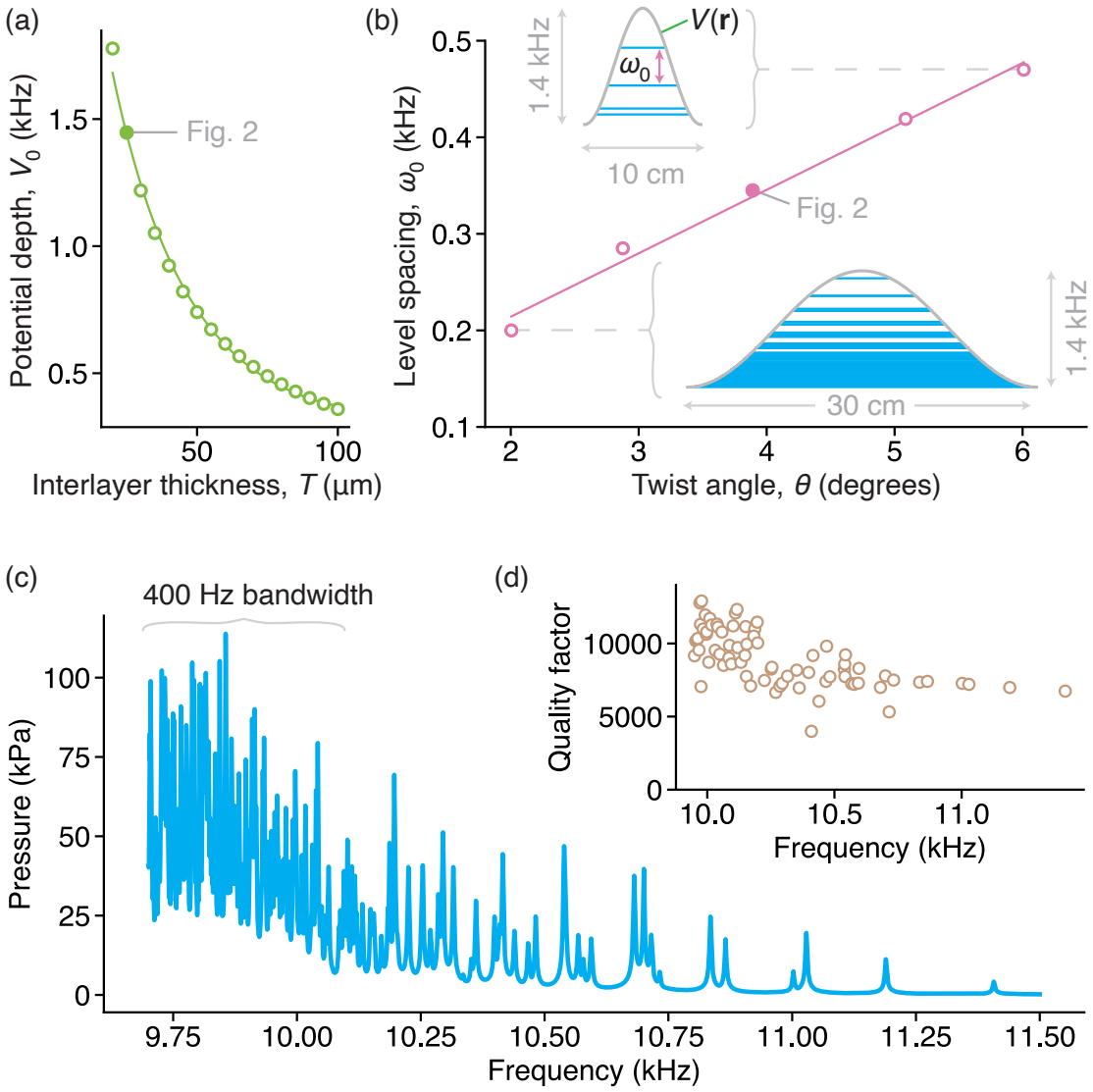

Figure 4.3: Tuning the properties of an acoustic harmonic resonator. a, The depth, V_0, of the AA-centered potential well grows with reduced interlayer thickness. The thickness $T = 25\,\mu$m used in Fig. 4.2 lies in the strong coupling regime where many harmonic oscillator states are visible. **b,** The spacing between the lowest two harmonic oscillator states, ω_0, grows linearly with twist angle θ, at fixed $T = 25\,\mu$m. The potential (gray line in insets) widens at lower twist angles, allowing more harmonic oscillator modes (blue lines) to form. **c,** At $\theta = 2^\circ$, the ladder of harmonic oscillator states appears as a series of closely-spaced, sharp peaks in the pressure response amplitude as a function of source excitation frequency. The higher angular momentum modes become densely packed in frequency, creating an effective 400 Hz bandwidth resonance response. The absolute amplitude of the peaks is dependent on the method of excitation, in this case, eight point sources placed in cavities throughout the moiré cell. **d,** The corresponding Q values for the peaks in panel **c**, obtained by fitting a Lorentzian curve to each resonance and calculating the ratio of the amplitude to the full width at half maximum, remain greater than 4000 for all modes.

vesting [91], chemical and biological sensing [92], and second-harmonic generation [93, 94, 95, 96]. Moreover, although our simulations focus on macroscopic length scales and kHz frequencies, the underlying principles of moiré localization extend naturally to surface acoustic[97, 98, 99, 100] and photonic systems[101, 70, 102, 103], opening doors for novel microwave and optical devices.

5

Acoustic obstructed atomic insulator

The atomic insulator is well-described as a crystal with a full valence band and a finite energy gap to an empty conduction band. A simple corresponding real-space picture is given by the Fourier transforms of momentum-space energy bands, called the maximally localized Wannier functions (MLWF). In materials where this simple picture breaks down and the MLWF of a band cannot be exponentially localized to any point in the unit cell without explicitly breaking a symmetry or closing an energy gap, we say that the insulator is topological[104, 105, 106, 107, 108, 109, 110, 111,

112]. Finally, there exists another type of insulator where the MLWFs are exponentially localized in the unit cell, but off of any individual lattice site, called an obstructed atomic insulator (OAI) [111]. Here, MLWFs are localized at the Wyckoff positions of chemically bonded molecular orbitals that fill both the valence and conduction bands. The hybridization of several atomic orbitals form an effective higher-symmetry orbital spread across the unit cell, away from individual atoms. As a result, even non-interacting particles can be sensitive to the occupation of other nearby modes.

The interdependence of modes within the unit cell in an OAI leads to a bulk-boundary correspondence if the effective higher-symmetry orbital is disrupted. In contrast, the bulk-boundary correspondence of a topological insulator is global and guaranteed by continuity of the wavefunction, giving rise to a conducting boundary and an insulating bulk. When the molecular orbitals of an OAI are cut by two conjoining boundary terminations, dangling bonds lead to corner-localized 0-D states, similar to the conducting states of a higher-order topological insulator [113]. However, attempts to visualize this phase have been hindered by limitations in microscope resolution. Moreover, corner states can be difficult to observe, as impurities, long-range hopping, and edge reconstruction can push them into the manifold of bulk states [114, 115, 116].

In general, OAIs have dispersive valence and conduction bands which can overlap with other trivial states. Delocalized excitations and interference from nearby bands makes real-space imaging of the molecular or in an OAI challenging. Therefore, the discovery of a clean 2D OAI system with an isolated, ultra-flat conduction band is particularly attractive, as a very localized wavefunction would be easier to identify. In real space, a non-degenerate flat band manifests as a highly localized mode, called a compact localized state (CLS). Such a flat band has very small kinetic energy, making any interactions present in the system the dominate contributor to the Hamiltonian. Thus, electronic insulating flat bands could lead to the emergence of strongly correlated [117] and Mott physics [118] that are currently unexplored in the OAI regime.

In this work, we design the first 2D flat band OAI and experimentally implement it in an acous-

tic metamaterial. Our metamaterial embeds the "Star of David" motif, which typifies the (gapless) kagome flat band, in an extended triangular lattice. In our "extended-kagome" lattice, we isolate the same CLS that makes up the kagome flat band, but now protected by a gap to all dispersive modes. By exciting the acoustic modes of the system with a single point source, we derive the band structure of the system and observe a gapped non-degenerate flat band, an effect previously unseen in explorations of photonic or phononic engineered super-lattices [119, 120, 121, 122, 123, 124, 125, 126, 127, 128, 129, 130, 131, 132]. In addition, unlike previous designs of metamaterial OAIs which have been characterized by quantized dipole [113] or quadrupole moments [133, 134, 135], the acoustic ext-kag lattice hosts quantized hexapole moments. Lastly, The high degree of tunability provided by acoustic metamaterials allows us to explore the ext-kag corner modes by breaking the unit cell symmetry with various boundary terminations. The observation of a 2D OAI with an ultra-flat conduction band points to a candidate lattice to observe overlap between strongly correlated physics and the OAI phase.

5.1 OAI in one dimension

One of the earliest and simplest examples of an OAI is the Su-Schrieffer-Heeger (SSH) [136] model. Consider a 1D chain of N atoms with alternating nearest-neighbor hopping strength $t_1 \neq t_2$. The band structures of the two atomic chains are shown in Fig. 5.1**b**, which can be derived through a simple tight-binding model. Intuitively, chemically bonding/anti-bonding orbitals create MLWFs of the valence band that are centered in between strongly bonded atomic pairs, as shown by the schematic diagram in Fig. 5.1**a**. The localized, symmetric, yet off-atom nature of the Wannier centers prove that the atom chain is actually an OAI[137]. The gray trace on top of the trivial phase diagram illustrates the charge-density distribution when the atomic chain ends with strongly bonded atomic pairs. In the non-trivial phase when the chain ends with weakly bonded atomic pairs, "half-

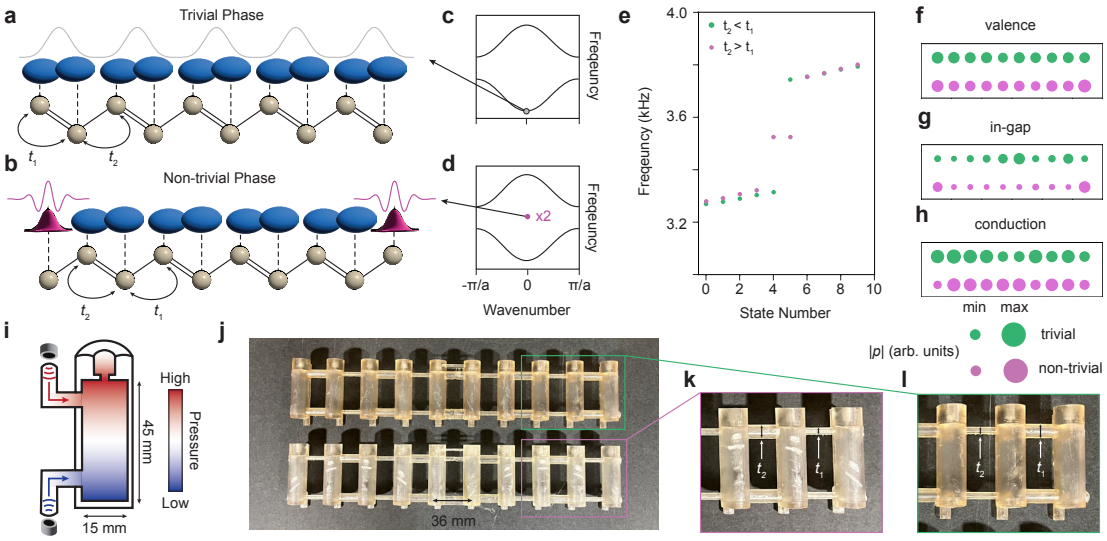

Figure 5.1: Realization of a one-dimensional acoustic OAI. a, The Su-Schrieffer-Heeger (SSH) model is a simple 1D example of an OAI. When a chain ends in between two weakly bonded atoms, it is in the trivial phase. The gray trace represents the wavefunction probability density for a simple bulk mode from the bands formed by the orbitals depicted as blue clouds. **b,** Meanwhile when a chain ends in between two strongly bonded atoms, it is in the non-trivial phase. The magenta traces represent the emergent edge modes. **c,** The band structure for the 1D SSH chain in the trivial phase. The gray dot is a bulk mode correspondingly to the gray trace in **a**. **d,** The band structure for the SSH chain in the non-trivial phase. The in-gap edge states are represented by the (two-fold degenerate) magenta points. **e,** COMSOL Multiphysics eigenstate simulation of the trivial (green) and non-trivial (magenta) phases. **f,** Experimental acoustic response of each cavity in both the trivial (green) and non-trivial (magenta) phase at a frequency above the gap in the valence band. Acoustic pressure response amplitude is linearly mapped to the area of the representing dot. **g,** Same as **f,**, but for a frequency in the band gap. **h,** Same as **f,**, but for a frequency below the gap in the conduction. **i,** Schematic diagram of the cavity acoustic resonators used in our experimental setup. **j,** Image of the 3D printed trivial(top, $t_1 > t_2$) and non-trivial (bottom, $t_1 < t_2$) phases of an acoustic metamaterial 1D OAI. **k,** Alternating channel widths are used to implement two different hopping strengths, so a non-trivial SSH chain terminates with the edge cavity weakly coupled to the rest of the chain. **l,** A trivial SSH chain terminates with the edge cavity strongly coupled to the rest of the chain.

orbital"s are created as edge charges. Such edge charge is the manifestation of quantized electric dipole moment defined as the sum of Wannier centers[138, 139],

$$\mathbf{p} = -\frac{e}{A}\sum_{i=1}^{N}\mathbf{r}_i \tag{5.1}$$

where e is the electric charge, A is the area of the unit cell, and $\mathbf{r}_i$ is the center of each MLWF. Equivalently, the quantized dipole moment is the Berry phase of the valence band[140, 141]:

$$\mathbf{p} = -\frac{e}{S} \oint_{BZ} i \langle u_k | \partial_k u_k \rangle \, \mathrm{d}k \tag{5.2}$$

where $|u_k\rangle$ denotes the eigenstate of the occupied band and S is the area of the 1st Brillouin zone. Solving the tight-binding model gives us the values of the two distinct phases of OAI[142]:

$$\mathbf{p} = \begin{cases} 0 & t_1 > t_2 \\ -\frac{e}{2} & t_1 < t_2 \end{cases} \tag{5.3}$$

the quantized value $-\frac{e}{2}$ clearly shows that the non-trivial phase manifests as a in-gap corner mode, as shown by the pink dots in Fig. 5.1**b**, while the bulk remains topologically trivial. The equivalence between these two concepts tells us that, intuitively, the bulk-boundary correspondence of the OAI is caused by breaking the localized MLWF and leaving excessive charge on the edge.

Our metamaterials consist of [143, 144, 145, 113, 146] coupled-acoustic resonator chain as shown in Fig. 5.1**c**. Each resonator imitates a single atomic site and is composed of three hollow cylindrical cavities as shown in Fig. 5.1**d**. The primary cylinder, with height 45 mm and radius 15 mm, is a Helmholtz resonator whose fixed resonance frequencies mimics the on-site energy of an atomic orbital. A smaller cylinder of height 3.5 mm and radius 0.5 mm forms a neck for the Helmholtz resonator where a microphone is placed to measure the acoustic response within the cavity. Lastly, a pair of cylindrical acoustic waveguides of length 7.5 mm and radius 2 mm connect to the sides of the excited cavities. A pair of transducers drives the resonator through these waveguides, exciting the fundamental mode with a π-phase shift along the long axis, an acoustic analog of a p_z orbital, as shown in Fig. 5.1**d**. The geometric parameters of the metamaterial were chosen to

maximize the quality factor of the acoustic response.

We 3D-printed two 10-resonator chains with different edge termination patterns (Fig. 5.1**c**). Resonators are coupled by cylindrical waveguides of fixed length but alternating radii of 1.5 mm and 3 mm, implementing two possible coupling strengths t_1 and t_2. The model is in the trivial phase if the edge coupling is weaker ($t_1 < t_2$), as is the case for the upper metamaterial in Fig. 5.1**c**, and in the non-trivial phase if the edge coupling is stronger ($t_1 > t_2$), as is the case for the lower model in Fig. 5.1**c**. Eigenstate calculations from COMSOL Multiphysics, shown in Fig. 5.1**e**, produce an expected band gap of 470 Hz for the trivial phase (green dots), while the non-trivial phase (pink dots) hosts two in-gap edge states. We experimentally verify the existence of such in-gap edge states by exciting each resonator individually and recording the acoustic response from the same resonator. The acoustic pressure distribution of the trivial and non-trivial phases are nearly identical for frequencies within the valence ($f = 3.300$ kHz) and conduction ($f = 3.770$ kHz) bands, as shown in Fig. 5.1**f**. Meanwhile, at the in-gap frequency ($f = 3.511$ kHz) there is very low acoustic response throughout the trivial chain, but a large acoustic response only at the edges for the non-trivial chain, indicating the presence of in-gap edge states and confirming the transition into the OAI phase.

5.2 OAI in two dimensions – extended kagome lattice

In 2D the picture becomes more complicated, but OAIs can still be formed by constructing a lattice that hosts off-atom, exponentially localized MLWFs. We create a novel 2D OAI by embedding the kagome unit cell in a larger triangular lattice, generating a gapped flat band with a MLWF localized to the center of the new unit cell. A conceptual diagram of the real-space mode corresponding to the flat band is depicted in Fig. 5.2**a**. In-plane *s*-like orbitals occupy the inner hexagon of the conventional "star of David" kagome cell, with alternating π phase shifts every other site. Together, these *s*-like modes form a single f_{xy}-like orbital occupying each "star of David". The symmetry of the

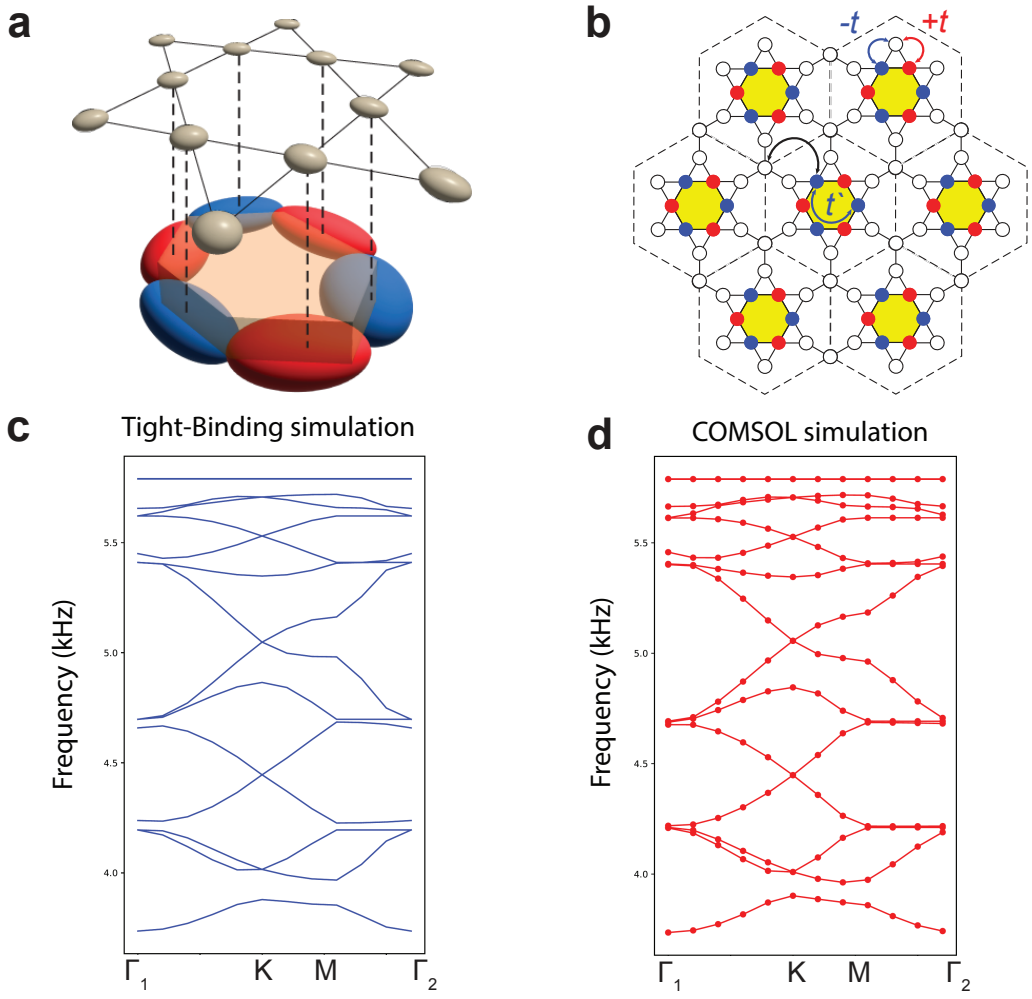

Figure 5.2: A 2D OAI with an isolated ultra-flat band. **a,** Diagram of the spatial distribution of the CLS of the ext-kag lattice at the flat band frequency. The alternating phase of the wavefuntion in the inner six sites cancels the nearest-neighbor hopping, t, outside of the inner hexagon, localizing the mode. **b,** The CLS tiles out across the lattice to generate an emergent triangular lattice of obstructed atomic f_{xy} orbitals. **c,** A tight-binding model with nearest-neighbor and small next-nearest-neighbor hopping ($t \neq t' \neq 0$) gives rise to a flat band that overlaps with other dispersive bulk modes. Adding a small but finite onsite potential to the inner six sites of the unit cell then pushes the flat band above the dispersive modes, gapping it out. **d,** COMSOL calculated band structure for an acoustic metamaterial analog of the the extended kagome lattice.

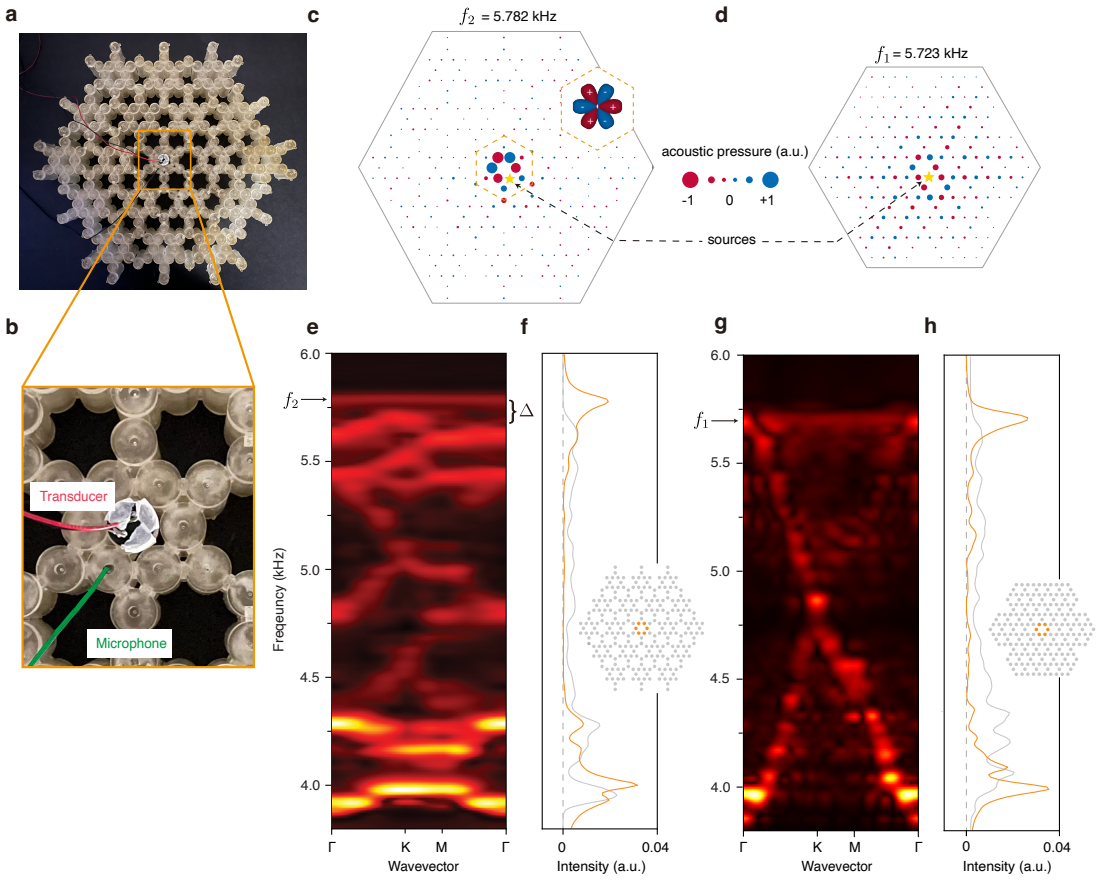

Figure 5.3: Realization of two-dimensional acoustic OAI in an extended kagome lattice. a, Image of the 3D printed extended kagome acoustic metamaterial lattice. **b,** Zoom-in of the central unit cell of the metamaterial shown in **a**. The transducer used to excite the acoustic modes and the microphone used to measure the response are shown. **c,** The measured real space distribution of the flat band in the extended kagome lattice. The resonator containing the acoustic transducer is indicated by a gold star. Acoustic response is linearly mapped to the area of the representing dot. **d,** Same as **c**, but for the kagome metamaterial. **e,** The measured band structure and **f,** density of states (DoS) of the extended kagome acoustic metamaterial. The yellow DoS curve is averaged over six cavities in the central unit cell where the transducer is placed while the gray DoS curve is averaged over the rest of the system. **g-h,** Same as **e-f**, but for the kagome metamaterial.

hexagon is such that the nearest-neighbor hopping, t, to the sites on the edges of the "star of David" destructively interfere, giving no spectral weight on those sites, as shown in Fig. 5.2**b**. Thus, the flat band forms a new triangular lattice of the effective f_{xy} orbitals, strongly localized at the center of

each unit cell.

The true advantage of the extended kagome lattice is only revealed when next-nearest-neighbor hopping, shown as t' in Fig. 5.2**b**, is considered. The flat band of the traditional kagome lattice has a time-reversal symmetry protected degeneracy at Γ with the highest dispersive band. Therefore, although it exhibits a similar spatial wavefunction distribution, this mode is not a CLS. The introduction of the extra lattice site in the extended kagome at the edge of each "star of David" expands the number of bands from 3 to 14, as shown in tight binding calculation Fig. 5.2**c**, giving the degrees of freedom for the orthonormal basis to contain a gapped flat band, no longer protected by TRS [147]. This has two primary advantages: I) the gap can be tuned by an onsite potential, δ, on the inner six sites of the unit cell and II) the symmetry of the flat band mode negates next-nearest-neighbor hopping effects, since all second nearest neighbors are either perfectly in phase or have no spectral weight to contribute. In the acoustic metamaterial, naturally $\delta \neq 0$ by virtue of the coupling channels, which slightly increase the volume of the inner 6 cavities, which have 4 coupling channels each, compared to the outer 8, which have only 3 each. This leaves the frequency of the flat band nearly unchanged when $t' \neq 0$, while all other modes are driven down in frequency, as shown by the COMSOL simulation in Fig. 5.2**d**.

We experimentally verify the existence of the gapped flat band of the extended kagome lattice shown in Fig. 5.3**a**. Acoustic resonators are arranged into the 14-cavity unit cell of the extended kagome lattice with identical geometric parameters as used for the 1D SSH metamaterial model. In order to measure the relative phase difference between each resonator, the source is fixed at a resonator inside the central unit cell, shown in Fig. 5.3**b**. For each excitation frequency The real space distributions of acoustic pressure are measured by a microphone. The expected CLS associated with the extended kagome flat band appears as a large relative amplitude with alternating phase on the inner hexagon of the excited unit cell, as shown in Fig. 5.3**c**. Each circle represents an acoustic resonator, with the area scaling with acoustic pressure and the phase color-coded. The phase infor-

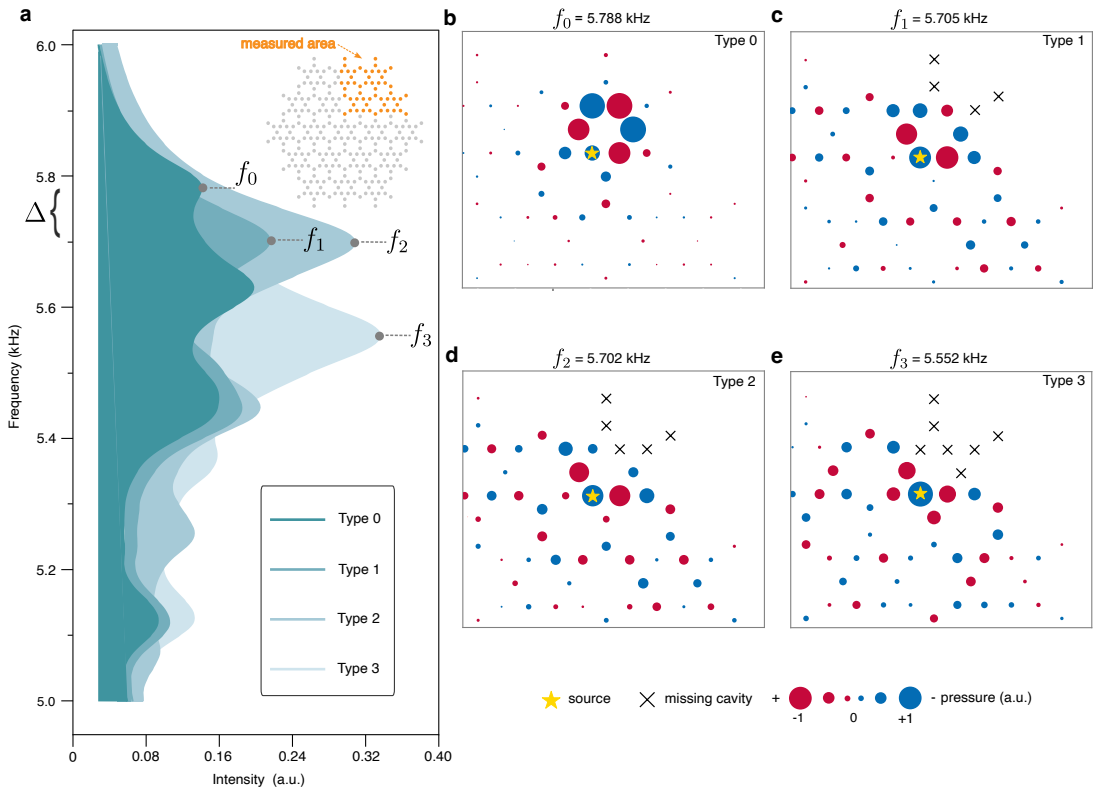

Figure 5.4: Corner terminations create edge-localized modes in the ext-kag OAI. a, The DoS for four types of corner terminations for the extended kagome lattice averaged over the corner of the lattice highlighted in the inset. Different shades of blue correspond to different measured corner terminations. Peaks in the DoS associated with the corner defect modes are indicated by gray dots. **a-d** Measured response amplitude of different corner terminations at the peak response frequencies labeled by f_0 – f_3 in **a**, respectively. **b,** The "natural" corner is a control for a perfected tiled unit cell with no extra missing cavities, leaving the flat-band mode unchanged at f_0. **c,** A corner termination removing 4 cavities from the outer unit cell protects the hexagon that hosts the obstructed f_{xy} orbital, shifting the flat-band peak down to f_1, but still above the bulk bands. **d,** A corner with 5 missing cavities slightly disrupts the OAI flat band mode, turning it into a defect corner state at $f_2 \sim f_1$. **d,** A corner termination with 7 missing cavities cuts the inner hexagon in half, greatly disrupting the OAI state and generating a corner defect mode deep in the bulk at f_3.

mation allows us to Fourier transform and reconstruct the extended kagome metamaterial's band structure, as shown in Fig. 5.3**e**. For comparison, the same measurement was taken on an analogous geometry kagome metamaterial at the flat band frequency, as shown in Fig. 5.3**d**, and its band structure is visualized in Fig. 5.3**g**. For both metamaterials, the expected spatial symmetries of the kagome

CLS are observed at their respective flat band frequencies ($f_{\mathrm{FB}}^{\mathrm{k}} = 5.732$ kHz and $f_{\mathrm{FB}}^{\mathrm{x\text{-}k}} = 5.782$ kHz), with further localization to the central unit cell in the extended kagome lattice. The large resonance amplitude within the central unit cell where the source resonator is located, in conjunction with the shorter decay length, indicates that bulk modes are not simultaneously excited and therefore gapped.

From the band structure, it is apparent that there is a $\sim$ 100 Hz band gap between the very sharp flat band at the top of the spectrum and the closest dispersive modes. To further characterize this gap, we plot the local density of states of both the extended kagome and kagome metamaterials, as shown in Fig. 5.3**f,h**, respectively. The yellow curves show the local density of states of the innermost hexagon of the central unit cell, and the gray curves are an average over the rest of the metamaterial. For both systems, the exact flat band frequencies can be derived from the center of the highest frequency response peak in the yellow curve. The gray curve in Fig. 5.3**h** has finite value at $f_{\mathrm{FB}}^{\mathrm{x\text{-}k}}$, but the gray curve in Fig. 5.3**f** dies rapidly just below $f_{\mathrm{FB}}^{\mathrm{x\text{-}k}}$, indicating the bulk dispersion band terminates before reaching the flat band in the extended kagome lattice, further supporting the existence of a gapped flat band in the extended kagome lattice.

We further prove that the flat band of the extended kagome lattice is in the OAI phase by altering its corner termination. A key signature of an OAI is the emergence of in-gap states when the wavefunction of the localized mode is disturbed by a defect, as was the case in the 1D SSH model (Fig. 5.1**d**). Here, we modify the corner unit cell of the extended kagome lattice by altering the corner termination of the finite metamaterial in 3 different ways, shown in Fig 5.4 **b-e**), which we name Type-0, 1, 2, 3 termination. Each missing cavity is marked by an "x". All corner unit cells are excited from the same relative cavity (marked by the yellow star). For each termination type, a local part of the metamaterial is measured, shown in orange in the inset of Fig. 5.4**a**. For each measurement, an average of the acoustic response is shown by the different shades of blue curves shown in Fig. 5.4**a**. Each response curve has a peak associated with a mode relatively localized to the corner

cell, marked by the gray dots and labeled $f_0 - f_3$. The peak positions move down in frequency as the number of missing cavities in the unit cell increases. It is important to note the absence of the original flat band peak from the Type 1,2,3 terminations, indicating that the missing cavity does not destroy the flat band, but rather it manifests as a corner defect mode at lower frequencies.

We theoretically propose a flatband OAI in 2D, a new class of topologically-trivial insulator, and experimentally realize it by engineering a novel lattice in an acoustic metamaterial. We observe various corner terminations that intersect the Wannier center of the CLS and track the resulting change in frequency of the flat band. Our precise control over acoustic metamaterial geometries allow us to study the features of 2D OAIs, and would help lead to faster progress in novel quantum materials.

6

Designer surface acoustic waves

The propagation of mechanical waves along the surface of some piezoelectric materials, called surface acoustic waves (SAWs), provides a pathway for direct conversion between mechanical, electrical, and optical energy, making the phenomenon suitable for applications in microwave technologies. SAWs have several advantages over other classical wave platforms for microwave applications, including ease of electrical excitation up to tens of GHz, micron wavelengths allowing for miniaturization, and the potential for low loss transmission [148]. Microfabrication on the surface of

$LiNbO_3$ allows for the scattering of the traveling waves into standing waves to create strong resonators [149, 150, 151, 152], as is needed for opto-mechanical conversion or signal amplification. Alternatively, coupling travelling SAWs to quantum systems [153, 154, 155, 156] opens the doors for uses in quantum communication or information processing technologies. For many applications, advanced band structure engineering is required, making metamaterials an ideal platform to achieve the desired SAW dispersions. However, tools for direct measurement of travelling SAWs is lacking, making it difficult to design and test the engineered lattices.

It is well known that acoustic metamaterials, systems whose dispersion properties are determined by macroscopic geometry as oppose to that of their constituent parts, have been used to great success to control sound waves. Complex wave dispersions such as topological insulators [70, 91, 157, 158, 159, 160, 98, 161], acoustic logic gates [71, 72], and materials with zero or negative refractive index [103, 74, 75] have been studied for sound in the audible or ultrasonic regime. However, the miniaturization of acoustic metamaterials to micron scales and microwave frequencies presents challenges in both fabrication and measurement. There has been previous effort to implement a metamaterial honeycomb lattice of deposited metallic micropillars to emulate the "massless" Dirac dispersion [97] or the topological features of sub-lattice symmetry breaking [98, 162, 163] in SAWs, but all have relied solely on transmission measurements or single frequency scanning readouts, leaving out much information about the SAW scattering mechanisms and behavior beyond the K point. Additionally, experimental measurements that rely on optical interference have a low spatial resolution limited by the spot size ($\sim 10\,\mu$m) and generally are sensitive to standing waves only.

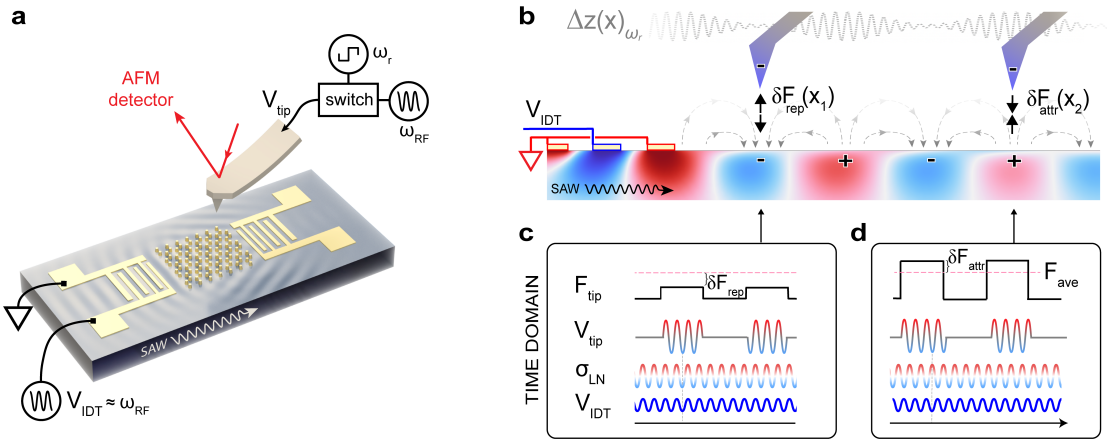

Figure 6.1: | **Metamaterial design a,** Optical image of a single SAW metamaterial device. A hexagonal lattice of 400 nm tall gold pillars is deposited in between two sets of interdigital transducers (IDTs) used for SAW generation/detection in the 880-1150 MHz frequency range. The SAW propagation direction corresponds to the x crystal axis of the 128° y-cut $LiNbO_3$ substrate. **b,** SEM image of the metamaterial. The direction of SAW propagation is k_x, which corresponds to the Γ — K direction of the honeycomb lattice. **c,** SEM picture of the pillars, where the white rhombus indicates the unit cell, which consists of two deposited gold nanopillars. Parameters in the figure are $a_0 = 1.06\,\mu$m, $r_0 = 300$ nm, $h = 400$ nm, and δr varies among different samples depending on the degree of intended sublattice symmetry breaking, i.e., for a honeycomb lattice $\delta r = 0$. **d,** Simulated acoustic band structure of the graphene ($\delta r = 0$) metamaterial using COMSOL Multiphysics. The darker color corresponds to *Surface Modes*, while lighter color associates to *Bulk Modes*. The flat bands around 950 MHz come from the radial expansion of the pillars and it is decoupled from the substrate, thus it does not appear in the experiment. **e,** Simulated acoustic band structure of the h-BN metamaterial ($\delta r = 2$ nm) showing a band gap of 40 MHz around the K point.

6.1 Introduction to Electric force microscopy (EFM)

Here we present the use of electrostatic force microscopy (EFM) [164, 165, 166] as a platform for the study of SAWs metamaterials. The large bandwidth and sub-micron spatial resolution capabilities of EFM gives access to direct k-space measurements, making comprehensive studies of SAW metamaterial band structures more accessible than ever before. As a proof of concept, we deposit a honeycomb lattice of Au pillars on the surface of $LiNbO_3$, reproducing the expected Dirac dispersion around the K point. We observe a significant reduction of the speed of sound near the Dirac point as well as scattering from the excitation axis into the three-fold rotation symmetry axes of the hexagonal unit cell. Additionally, we reproduce the full band structure within the honeycomb

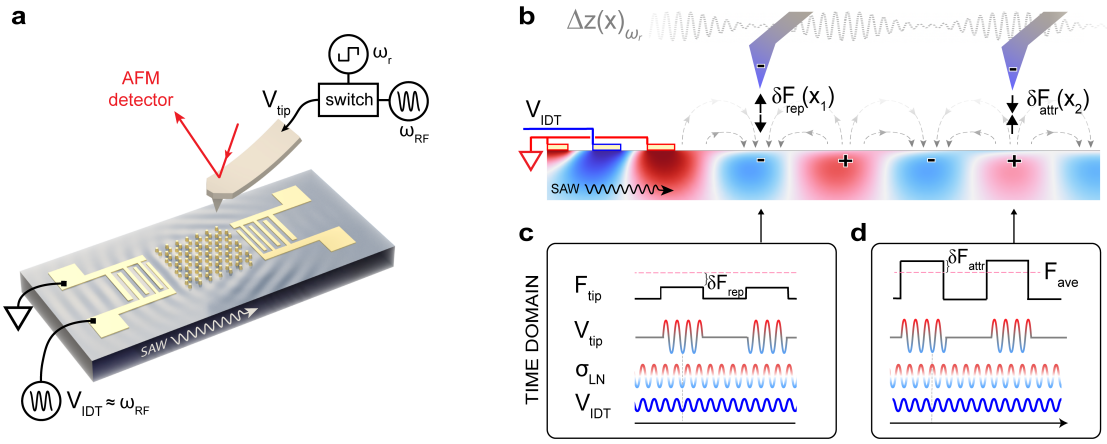

Figure 6.2: A novel platform for the design and measurement of SAW metamaterials. **a,** Schematic of experimental setup including the metamaterial device and the electrostatic force microscope (EFM) used for the detection of the traveling SAWs. The EFM is a modified optical detection conductive AFM system that applies the RF voltage used to drive the IDTs to the cantilever, chopped by its resonant frequency, ω_r. The nonlinear interaction between the probe and substrate effectively down-converts the response of the high-frequency component to an amplitude at the mechanical resonant frequency of the cantilever (cite). **b,** Snapshot in time of the tip-sample interaction mediated by the surface charge build (sigmaln) up of the SAWs. At points on the surface where the phase difference between the RF signal at the tip (V_{tip}) and the charge wave associated with the SAW σ_{LN} is $n\pi$ for an integer n, the force will be maximally repulsive for even n, as is the case at position $x = x_1$, or maximally attractive for odd n, as shown for $x = x_2$. The resulting magnitude of the force felt by the cantilever $|F_{\text{tip}}|$ is a sum of both a spatially dependent force contribution $\delta F(x)$, which depends on the phase of the SAW, and a background attractive electrostatic force, F_{ave}, that remains constant as a function of x. **c,d** Time evolution of sample-tip interaction at $x = x_1$ (and $x = x_2$), where the force is maximally repulsive (or attractive), resulting in minimal (maximal) oscillation amplitude $|\Delta z|_{\omega_r}$.

metamaterial over a wide bandwidth ($\sim$ 280 MHz), not previously accessible by other scanning methods. We observe a transition from the ballistic to the diffusive scattering regime as the frequency crosses above the *K*-point, revealed by a significant drop in the signal-to-noise (S/N) ratio, supporting the existence of "deaf" bands [97, 167]. Additionally, we open a tunable gap around the Dirac point by breaking sub-lattice symmetry, reinforcing the power of this platform for arbitrary SAW band engineering.

Our SAW metamaterial is composed of metallic pillars arranged in a honeycomb lattice on a piezoelectric 128°-Y cut bulk $LiNbO_3$ substrate. Figures 6.1 b and c show scanning electron microscopy (SEM) images of a fabricated metamaterial, where gold (Au) pillars were fabricated using

electron beam lithography and deposition (see Methods). This metallic array of micro-resonators induces periodic potential variations in the SAWs. Each pillar acts as a local resonator coupled to the $LiNbO_3$ substrate, thereby mimicking electronic dispersion in 2D hexagonal quantum materials [168, 97]. The rhombic primitive cell of our SAW metamaterial contains two sublattice sites, A and B, which are micro-pillars with equal height (h$\sim$ 400nm) and sidewall angle ($\theta \sim 18°$). When sublattice sites A and B have equal radii, the structure can be viewed as an acoustic analog of graphene. The C_6 symmetry of the honeycomb lattice preserves the SAW Dirac degeneracies around the K and K' points of the first Brillouin zone, analogous to graphene. By introducing a difference in the radius of the pillar between the sublattice sites, the symmetry of the lattice is reduced to C_3. The broken inversion symmetry lifts the Dirac degeneracy, inducing a band gap. Two broadband interdigital transducers (IDTs) capable of generating planar SAWs ranging from 850 MHz to 1150 MHz are patterned on the same substrate, launching waves in the x-crystallographic direction of $LiNbO_3$.

Electrostatic Force Microscopy (EFM) achieves sub-micron resolution over a broad bandwidth (500 MHz-1500 MHz), employs an heterodyne technique that circumvents direct RF signal detection and allows for the visualization of traveling waves. Furthermore, being a non contact mode, it allows for fast scanning and finally can be implemented cheaply in most commercial AFM setups. For these reasons, EFM was chosen as the platform for SAW detection in our $LiNbO_3$ metamaterials.

The electrostatic force between the sample and the cantilever can be expressed as:

$$F_z(x, y, t) = \frac{1}{2}\left(\frac{\partial C_{ts}}{\partial z}\right) V_{tip}^2 + E_{tip} q_{tip} \tag{6.1}$$

Where C_{ts} denotes the sample-tip capacitance, V_{tip} is the tip voltage, E_{tip} is the electric field experienced by the probe as a result of the surface polarization and q_t is the amount of charge accumulated on the tip. The voltage applied to the tip is an AC voltage at the SAW frequency ω_{RF}, chopped by

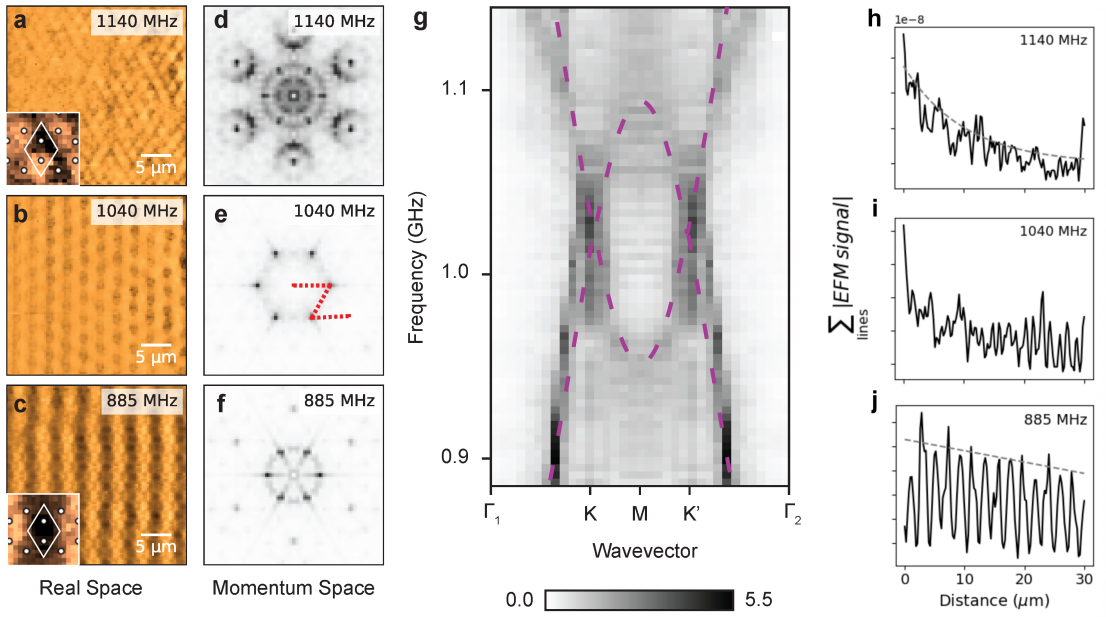

Figure 6.3: Direct observation of a Dirac cone in a SAW band structure. a-c, Amplitude of the EFM response over a $30 \times 30\,\mu$m scan frame for a frequency above (**a**), at (**b**), denoted f_K, and below (**c**) the K point. The SAWs are clearly visible in **c** and form the expected 2D hexagonal pattern at the K point in **b**. In **a**, the signal drops off as the symmetry of the modes above the K point prevents direct excitation with a plane wave, which we call "deaf" modes. The inset in (**a**) and (**c**) shows a zoom on the unit cell, where we observe respectively a bonding (**c**) and antibonding (**a**) mode. **d-f,** The Fourier transform of the real space images in **a-c**, respectively. **f** shows peaks expanding out along the Γ-K direction as frequency increases up to f_K. At f_K, there is a clear sixfold peak at the edge of the first Brillouin zone at all K/K' points, shown in **e**. The deaf modes are then visible above f_K in **d** as circular bands closing around Γ_2, as expected for a parabolic dispersion. The dotted red line in **e** shows the linecut along the Γ_1-K-M-K'-Γ_2 direction that generates the band structure in **g**. The cut extends into the second Brillouin zone as we measure momentum space directly with no band folding. **g,** The reconstructed band dispersion from the FTs show Dirac cones characteristic of a honeycomb lattice are visible at the K/K' points. The dotted magenta line is a tight-binding model meant as a guide to the eye. **h-j,** Sum of the spatial decay of EFM signal amplitude over all horizontal line scans from the real-space data in **a-c**. The observed exponential decay for frequencies above the K point indicates that driving of the deaf modes is likely through secondary scattering effects, resulting in a diffusive behavior. Below the K point, the SAW transport is ballistic resulting in a linear amplitude decay. A transition between the two behaviors is observed at f_K.

the cantilever resonant frequency ω_r. The tip voltage can be expressed as $V_{\text{tip}} = [0.5 + 0.64\ \cos\omega_r t] \times V_{\text{RF}} \cos(\omega_{\text{RF}} t)$, where the terms in the square bracket represent the fundamental harmonic of the chopping square wave.

For a propagating SAW in the $\hat{x}$ direction, we can drop the y dependence and approximate the

electric field at the cantilever tip due to the SAW as, $E_{\text{tip}}(x,t) = \sigma_{\text{LN}}(x,t)/\varepsilon_0 = \sigma_0 \cos\left(\omega_{\text{RF}} t + 2\pi x/\lambda\right)/\varepsilon_0$ where sigmaln is the local charge density, λ is the SAW wavelength and σ_0 is the magnitude of the charge density induced by the SAW. The charge accumulated at the tip, q_{tip}, can be approximated as the sum of the induced charge by the SAW plus the charge due to sample-tip capacitance: $q_{\text{tip}} = -\sigma_{\text{LN}}(x,t) + C_{\text{ts}} V_{\text{tip}}$. The total force on the cantilever can then be computed from Equation 1, substituting the terms discussed above. Due to the resonance behavior of the cantilever, the displacement amplitude is a function only of the terms that have an ω_{r} time dependence, and any RF frequency will be effectively integrated as the cantilever does not respond high frequency perturbations. Finally the cantilever displacement is proportional to:

$$|\Delta z|_{\omega_{\text{r}}} \propto \left| \overbrace{\frac{C_{\text{ts}}\sigma_0}{\varepsilon_0} V_{\text{RF}} \cos\left(\frac{2\pi}{\lambda} x\right)}^{\delta \text{F}(x)} + \overbrace{\frac{1}{2}\frac{\partial C_{\text{ts}}}{\partial z} V_{\text{RF}}^2}^{\text{F}_{\text{ave}}} \right|_{\omega_{\text{r}}} \tag{6.2}$$

Where the first term arises from the net attractive δF_{attr} of repulsive δF_{rep} force contribution and it is a function of the spatial SAW phase $(\frac{2\pi}{\lambda}x)$ while the second term is the background spatially independent attractive force contribution F_{ave}, as depicted in the schematic in Figure 2.

In our experimental setup, a Platinum (Pt) coated cantilever (Olympus OMCL-AC240TM, spring constant $k = 2\,\text{N/m}$, quality factor in air $Q \approx 200$) was used to scan at a constant height of 180 nm above the sample surface. Each $30 \times 30\,\mu$m scan is acquired in approximately 2 minutes, with a spatial resolution of 230 nm per point. The spatial resolution of EFM is estimated to be on the order of the tip-sample distance [166]. The scanning procedure consisted of two distinct phases: first, an Alternating Contact (AC) mode line scan was performed to acquire the sample topography. This was followed by a "lift-mode" line scan at the predefined height. During the lift-mode scan, the cantilever was not mechanically driven; instead, the oscillation amplitude was due solely

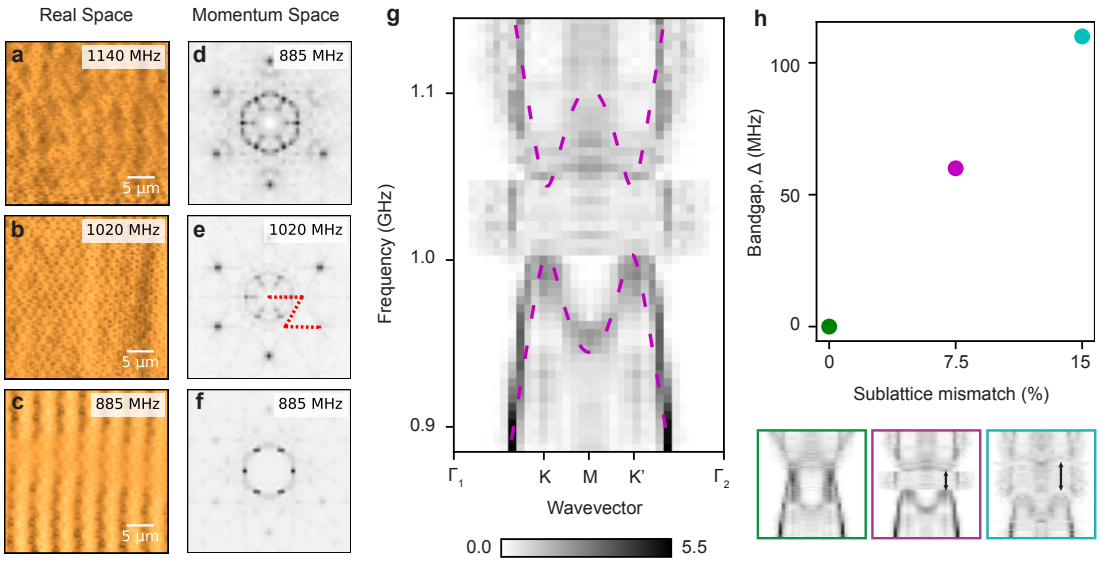

Figure 6.4: | **SAW band gap is tunable. a-c,** EFM amplitude over a $30 \times 30\,\mu$m scan range at **a,** 1140 MHz, above f_K, **b,** 1020 MHz, at f_K, and **c,** 885 MHz, below f_K in an h-BN SAW metamaterial analog with $\delta r = 15$ nm. **d-f,** Fourier transform of the images in **a-c**. Clear peaks in the first Brillouin zone (**f**) move towards the edge of the K point at f_K (**e**) and then move into the second Brillouin zone above f_K (**d**). Note the absence of the bright peaks at the edge of the Brillouin zone at f_K compared to the graphene metamaterial in Fig. 6.3 e. The dotted red line in **e** shows the linecut along the $\Gamma_1 - K - M - K' - \Gamma_2$ that generates the band structure in **g. g,** A band gap of 50 MHz opens around f_K due to the sublattice symmetry breaking. Two dispersive bands are still visible above and below the gap. The dotted magenta line is a tight-binding model meant as a guide to the eye. **h,** The width of the SAW band gap is proportional to the induced sublattice mismatch, with green, purple, and teal representing a mismatch of $\%0$, $\%7.5$, and $\%15$ respectively.

to the electrostatic interaction between the tip and the sample. The 180 nm lift height was chosen to achieve a balance between maximizing the signal-to-noise ratio and providing a sufficient height margin, preventing potential tip collisions with the pillars during the lift-mode EFM measurements. The datasets presented hereafter comprise EFM scans acquired every 2.5 MHz (for graphene sample) and 5 MHz (for h-BN samples). The chopping frequency was tuned to within 100 Hz of the cantilever's resonant frequency to optimize the EFM signal-to-noise ratio.

6.2 Surface acoustic wave (SAW) graphene

We use EFM to characterize a honeycomb lattice of deposited Au pillars on the surface of $LiNbO_3$ to create an analogy to the electronic dispersion of graphene in SAWs. Real-space EFM measurements at three frequencies representative of the three distinct SAW transport regimes below, at, and above the Dirac frequency are shown in Fig. 6.3 **a**-**c**, respectively. Below the Dirac point, clear wavefronts along only the excitation direction are visible in the EFM amplitude shown in Fig. 6.3 **c**, corresponding to sharp peaks along the $\Gamma_1 - K$ lines in the first Brillioun zone, shown in Fig. 6.3 **d**. As the frequency increases scattering remains low until the Dirac point, $f_K = 1040$ MHz, where the wavefronts now exhibit interference patterns along the three rotation-symmetric axis associated with the K-point, shown in Fig. 6.3 **b**. The Dirac frequency serves as a crossover point from more ballistic-like to diffusive-like transport. In this regime, referred to as Pseudo-diffusion, the energy flux becomes omnidirectional as the group velocity direction becomes undefined at exactly f_K [97] (See [41] for details). Above f_K, The signal-to-noise drops significantly, leaving little trace of the wavefronts along any dominant direction, as shown in Fig. 6.3 **a**. However, the Fourier transform of the real space image, shown in Fig. 6.3 **d**, reveals the formation of ring-like features around the Bragg peaks, which are also the center of the second Brillioun zone, which we label Γ_2. With momentum space information as a function of frequency, we reconstruct the band structure, shown in Fig. 6.3 **g**, along the $\Gamma_1 - K - K' - \Gamma_2$ high-symmetry linecut. We observe the characteristic linear dispersion of the Dirac cone at the K and K' points, but with a reduced group velocity of 2700 m/s compared to the typical speed of 3900 m/s for free-space SAW transport in $LiNbO_3$, establishing our ability to control and measure the k-dependence of the SAW dispersion as well as the group velocity.

Any finite level of SAW scattering in the honeycomb metamaterial will disperse excitation power from the IDT, reducing the amplitude of the EFM response deeper into the lattice. As a result, the real-space data used to recreate the band structure in Fig. 6.3 **g** was collected in a region within

20 μm of the metamaterial boundary to optimize the S/N ratio. The average EFM amplitude as a function of distance along the $\hat{x}$-axis is shown in Fig. 6.3 **h-j**, corresponding to the data shown in Fig. 6.3 **a-c**, respectively. Below f_K the amplitude of the EFM response decreases linearly with distance, as shown in Fig. 6.3 **j**, implying a small scattering rate relative to the 30 $\times$ 30μm scan window, consistent with ballistic transport. Above f_K, the EFM response amplitude decays exponentially with distance, as shown in Fig. 6.3 **h**, corresponding to the high-scattering diffusive regime. The pseudo-diffusive crossover between the two regimes occurs at f_K, as shown in Fig. 6.3 **i**, where the decay is more consistent with a higher order polynomial. Due to the rapid decay of signal, it is difficult to measure any modes in the diffusive regime via transport methods [97]. However, the spatial resolution and high sensitivity of EFM permits imaging of previously invisible modes.

The emergence of diffusive transport at higher frequencies lies in the nature of classical waves. Unlike condensed matter systems, there is no concept of a Fermi level in metamaterials, which must be driven to populate the available eigenstates. There is then two requirements to excite SAW modes within the metamaterial: frequency and spatial mode symmetry. Below f_K, the two pillars within the hexagonal unit cell oscillate together, with no relative phase in the direction perpendicular to the incoming wave propagation, which we call the symmetric modes, as shown in Fig. 6.3 **c** inset. Above f_K, the two pillars oscillate out of phase, with a node appearing between pillars, which we call the anti-symmetric modes, as shown in Fig. 6.3 **a** inset. The IDTs generate plane waves at a fixed drive frequency f_D, which project onto the available symmetric eigenstates. This leads to direct excitation of modes below f_K, resulting in a strong EFM response, as shown in Fig. 6.3 c). However, above f_K, the incoming wave cannot project onto the anti-symmetric states, and therefore appear as an effective band gap, called "deaf" bands [167]. This has prevented previous experiments on honeycomb SAW metamaterials from observing modes above f_K. However, secondary scattering effects can still drive the anti-symmetric modes, but at much lower amplitude, requiring a measurement with high sensitivity. The SAWs measured by EFM are very clear below and at f_K, as shown in Fig. 6.3 c and

b, respectively. Meanwhile, above f_k, while the signal to noise is reduced, there is still clear signal, which allows us to reconstruct the dispersion relation of the upper band despite not being able to excite it directly. Thus for waves

6.3 Opening a controllable gap

The natural extension of tuning the SAW group velocity is control over the frequencies where SAWs can propagate at all. Breaking the six-fold rotational symmetry of the honeycomb lattice removes the protection of the Dirac cone, opening a gap in the energy spectrum. We tune the sublattice symmetry breaking through the difference in radius, δ, of the deposited Au pillar between the A and B triangular sublattices, creating a SAW metamaterial in analogy to hexagonal Boron Nitride. With a $\%7.5$ mismatch between sublattices, frequencies significantly above and below f_K behave similarly to the the case for SAW graphene, as shown in Fig. 6.4 **a,b** and **c,f**, respectively. However, frequencies near f_K now exhibit the behavior of a band gap, with no visible waves in the image shown in Fig. 6.4 **b** and corresponding pronounced Bragg peaks in the Fourier transform shown in Fig. 6.4 **e**. We can better visualize the behavior around f_K through the band structure along the $\Gamma_1-K-K'-\Gamma_2$ high-symmetry linecut, shown in Fig. 6.4 **g**. A spectral gap opens of $\sim$ 50 MHz around f_K, corresponding to a region of extremely rapid exponential decay of SAW amplitude into the metamaterial. Where eigenstates above the gap still can be excited via secondary scattering processes, there are no longer valid states for the incoming SAWs to project onto in the gap, preventing their propagation completely.

Sublattice symmetry breaking acts like a mass term added to the Dirac dispersion, with the added mass correlating with the level of symmetry breaking. Increasing the difference in pillar radius then serves as a tuning knob for the gap around f_k, as shown in Fig. 6.4 **h**. When the sublattice symmetry breaking is increased to $\delta = \%15$, the gap approximately doubles to $\Delta \sim 100$ MHz, represented

by the cyan dot, compared to the $\Delta \sim 50$ MHz gap for $\delta = \%7.5$, shown by the magenta dot. Meanwhile, for $\delta = 0$ we recover the honeycomb metamaterial with no gap opening, highlighted by the green dot. This near-linear trend is confirmed by COMSOL Multiphysics simulations shown by the crosses of the corresponding colors. We then have established the tunable transition between three regimes of SAW transport through the honeycomb metamaterial, ballistic, diffusive, and full reflection.

We have established a new platform for the design and measurement of GHz SAW metamaterials on the surface of piezoelectric crystals. A deposited lattice of gold pillars modifies the dispersion of incoming SAWs to implement an arbitrary tight-binding model determined by the geometry of the metamaterial. The spatial and frequency resolution provided by EFM enables us to directly image momentum space within the metamaterials and thus to recover the full band structure. We have demonstrated the ability to slow and completely gap out SAWs through this method of microwave band engineering. Additionally, we have established the tunable transition between three regimes of SAW transport through the honeycomb metamaterial: ballistic, diffusive, and full reflection, all with different scattering behaviors. This combination of metamaterial design and measurement allows for the more complex SAW band engineering for a variety of microwave technologies.

A

Twisted bilayer kagome lattice

A.1 Flat bands in solid state systems

The mechanism behind the high transition temperature of cuprate superconductors has been a driving question within the condensed matter field since the Nobel prize winning discovery of lanthanum barium copper oxide in 1986 [169]. Cuprates are strongly anisotropic bulk crystals, with much stronger bonds in-plane than between some planes. In particular, the CuO_2 planes form a

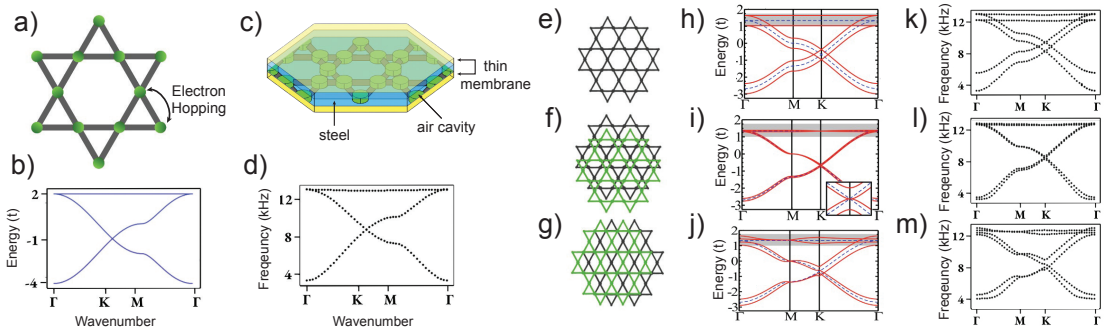

Figure A.1: Stacked kagome layers form a moiré pattern a, Geometry of a tight binding electronic kagome model displaying the star of David pattern. **b,** Lowest band manifold of the electronic tight-binding model for the kagome lattice. **c,** Geometry for the acoustic analog of the kagome lattice. Atomic sites are made from air cavities in a 1 mm thick steel sheet. Thin membranes are placed on the top and bottom to impedance match the system to air. **d,** COMSOL band structure calculation for the system with the unit cell shown in **c,**. The primary features including the Dirac cone at K and the flat band at the top of the spectrum is captured. **e-g,** Diagrams of the three possible high-symmetry stacking arrangements for bilayer kagome, C_6, C_3, and C_2, respectively. **h-j,** Electronic tight-binding band structure for the same three stacking arrangements [177]. **k-m,** COMSOL calculated acoustic band structure for acoustic bilayer kagome lattice with the same respective stacking orientations, capturing the same single-particle physics as the electronic tight binding model.

Lieb lattice, which hosts a quasi-2D flat band at the Fermi surface. The high superconducting transition temperature in cuprates has sparked wide interest in flat band materials in a search for other strongly correlated phases or clues about the mechanism behind superconductivity in cuprates. This search has lead to a recent interest in a class of crystals that contain 2D planes of atoms that form a kagome lattice. One such class are the kagome metals, such as KV_3Sb_5, CsV_3Sb_5, and RbV_3Sb_5 which contain a kagome net of vanadium atoms [170]. Several kagome metals have been shown to exhibit strongly correlated phases like superconductivity and charge ordering, including AV_3Sb_5 (for A=K,Cs,Rb) [171, 172, 173, 170], $CsTi_3Bi_5$[174], and ScV_6Sn_6 [175, 176]. The similarity of the flat band origin and the simultaneous emergence of strongly correlated states makes the kagome superconductors a potential key insight to the mechanism behind the unconventional cuprate superconductivity.

The search for flat band systems is not limited to bulk crystals, however. The discovery of Dirac cones transitioning to flat bands in magic angle TBG also leads to the emergence of strongly corre-

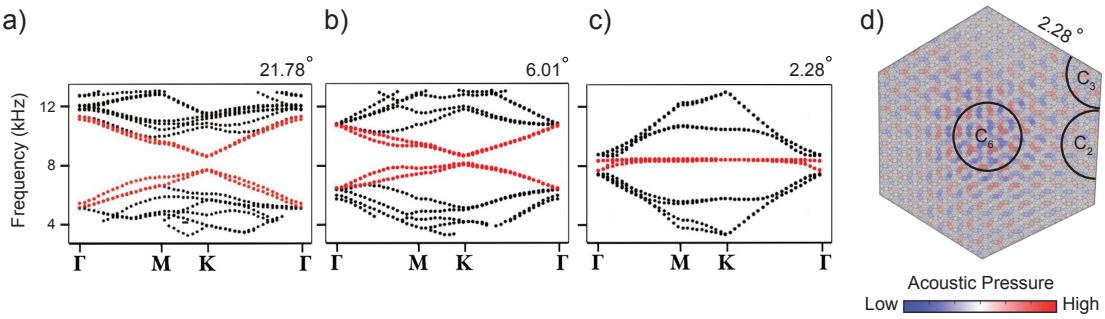

Figure A.2: Magic angle emerges in TBK. a-c, Calculated band structure around the Dirac frequency for a large (**a**), intermediate (**b**), and small (**c**) interlayer twist angle. The Dirac bands begin gapped out due to the interlayer hybridization but remain dispersive until a small enough twist angle where the bands become flat. **d,** Spatially localized mode corresponding to the lowest frequency flat band shown in **c**. The mode localizes around the AA stacking site where the interlayer hopping is the strongest.

lated states [66], and therefore may be important in understanding the cuprates as well. Flat bands have also been discovered in vdW heterostructures made from transition metal dichalcogenides [77, 78, 79, 80, 81], signifying the search for flat bands in vdW heterostructures is a greater property of moiré physics, and not exclusively to stacked layers of graphene.

There were several projects I began while in the Hoffman group that produced promising results, but we lacked the resources, time, or manpower to bring to fruition. The most well-developed of those projects was the simulation of twisted bilayer kagome (TBK). As opposed to each layer consisting of a honeycomb lattice, like in TBG, TBK consists of two stacked layers of kagome lattices. The kagome lattice adds a third triangular sublattice, as shown in Fig. A.1 **a**, to the honeycomb structure, reproducing the Dirac cones graphene is known for around the *K* point, but also hosting a new flat band that is degenerate with the highest energy dispersive mode at Γ, shown in Fig. A.1 **b**. Although an exfoliatable 2D kagome material remains elusive, there is much to be learned about moiré physics writ large, and for when a 2D kagome system is created on the quantum level.

A.2 Implementing acoustic bilayer kagome

We designed an acoustic metamaterial twisted bilayer kagome lattice where the Dirac band flattening occurs at a larger magic angle than for TBG. Similar to the acoustic TBG system discussed in Chapter 5, each 2D kagome lattice site consists of a cylindrical air hole (density 1.2 kg/m^3, speed of sound 343 m/s) in a steel sheet (density 7850 kg/m^3, speed of sound 5790 m/s), as shown in Fig. A.1 **c**, supporting single-cavity acoustic modes with frequency spacing set by the cavity size. We connect these modes through thin channels to allow nearest-neighbor intralayer hopping $t_{||}$, and focus on the lowest (s-band) manifold of states, whose dispersion closely mimics that of monolayer kagome [177], as shown in Fig. A.1 **d**. For a resonator in the audible range, we choose a cavity radius of $R = 3.5$ mm, nearest-neighbor spacing $a = 10$ mm and channel width $w = 0.875$ mm. We used a frequency-domain eigenstate study in the acoustic module of COMSOL Multiphysics with periodic boundary conditions placed on all sides of a single moiré supercell.

To implement an interlayer coupling strength t_z, we insert a 1 mm thick membrane between two vertically stacked kagome metamaterial layers. The couplings $t_{||}$ and t_z are controlled by the channel width and interlayer membrane density, ρ, respectively [87, 88]. The interlayer hybridization opens a gap dependent on the stacking arrangement, as shown in Fig. A.1 **k-m**. While both the thickness *and* the density of the interlayer tune t_z, reducing the density allows us to reach otherwise inaccessibly large values of t_z. It has been shown that the magic angle in TBG can be increased by applying pressure to the bilayer system [178, 179], forcing the layers closer together and therefore increasing the interlayer hopping [68, 180].

We first search for the first magic angle by fixing the coupling membrane density $\rho = 350$ kg/m^3 and reducing the twist angle, θ, from a large to a small value, transitioning the bilayer from the nearly decoupled to the strongly coupled regime, respectively, as shown in Fig. A.2 **a-c**. As the twist angel approaches the first magic angle at $\theta = 2.28°$, the Dirac bands are pushed towards the Dirac

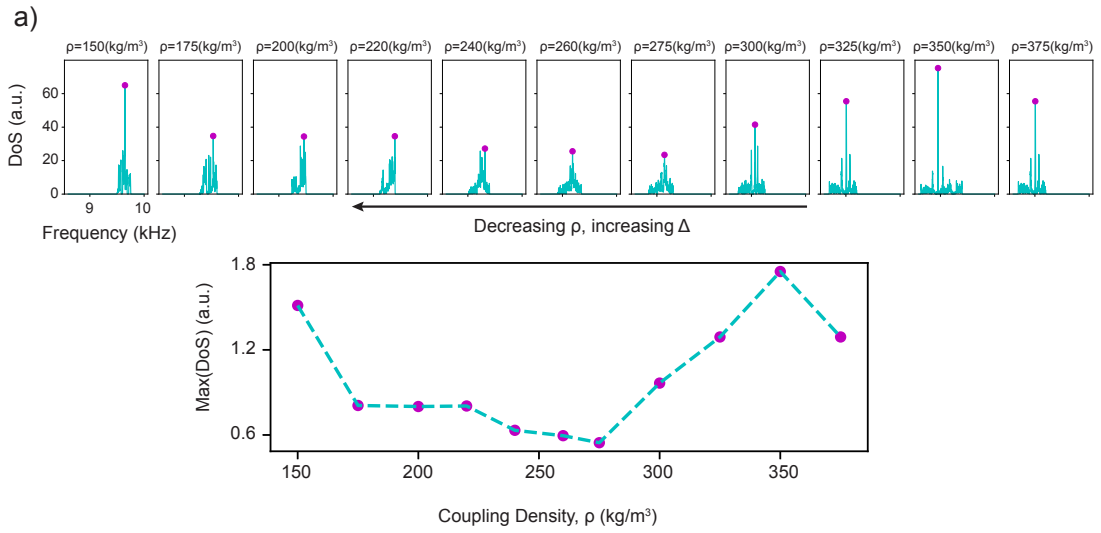

Figure A.3: DoS is a metric for identifying magic angles. a, Calculated Dos around the Dirac frequency for a range of interlayer coupling membrane densities, ρ, at a fixed twist angle, $\theta = 2.28^\circ$. As ρ decreases, t_z increases, raising the sequence of magic-angles. The maximum value of the DoS is marked with a magenta dot for each ρ value. **b,** The maximum of the DoS shows two peaks corresponding to the first two magic angles as ρ decreases.

frequency around 8 kHz, shown in Fig. A.2 **c**. The eigenstate associated with the Dirac bands is spatially centered and localized around the C_6 site in analogy to the localization to the AA sites in TBG.

A.3 Beyond the first "magic angle"

We often think of the "magic-angle" as the twist angle value at which we first see band flattening and corresponding strongly correlated behavior. However, the moiré supercell is defined by a larger length scale of $\lambda \sim \frac{a}{2\sin(\theta/2)}$ where a is the monolayer lattice constant magnitude, which means the Brillioun zone also shrinks by the inverse scaling factor. As a result, there are actually many "magic-angles" originating from the higher energy Dirac crossings generated by band-folding [68, 180]. The sequence of magic angles can be described by the dimensionless parameter $\alpha = \kappa \frac{t_z}{t_{||}} \sin(\theta/2)$, where for the kagome lattice $\kappa = \frac{2\sqrt{3}}{4\pi}$ [177]. Generally, the "magic angles" are where the hybridization

strength between the two layers cause maximal flattening of the Dirac bands and the physical signature of flat bands can be thought of as a reduced bandwidth [68]. Alternatively, the compression of spectral weight into a small bandwidth causes a spike in the density of states. The latter is a more convenient metric as it does not require keeping track of individual bands, but rather integrates over the whole Brillouin zone. We calculate a triangular cut of the sixfold symmetric Brillouin zone and choose an evenly distributed meshing to calculate the eigenfrequencies of the lowest band manifold. We then use a finite element method to integrate the band structure across the meshing to reproduce the DoS and integrated DoS.

The second magic angle is generally difficult to study due to the computational resources required to simulate a moiré system with the required small twist angle. Instead, we can fix the twist angle and realize a magic-angle through varying ρ. We see the first peak in the maximum value of the DoS, shown in Fig. A.3 **b**, at $\rho = 350$ kg/m^3, corresponding to the first magic angle, supporting the results shown in Fig. A.2 **c,d**. As ρ continues to decrease, the max of the DoS falls until it again peaks at $\rho = 150$ kg/m^3, indicating the existence of a second magic angle. It becomes difficult to explore the regime below $\rho = 150$ kg/m^3 as t_z becomes larger than $t_{||}$ and the bilayer tight binding model breaks down. Interestingly, the normalized max(DoS) for the second magic angle is larger than it is for the first, indicating the Dirac bands become even flatter. One possible explanation is the linear combination of the four Dirac bands can combine in a different way for the different magic angles, making the bands flatter. Alternatively, it is possible that the interlayer coupling has become so large in this regime that the original kagome flat band has been pushed down to the Dirac frequency due to the hybridization strength. We are still investigating which of these two competing solutions better explains the second peak in the max(DoS).

References

[1] B. H. November, J. D. Sau, J. R. Williams, and J. E. Hoffman, "Scheme for Majorana manipulation using magnetic force microscopy," *arXiv*, 2019.

[2] J. Shi, B. H. November, S. Carr, H. Pirie, and J. E. Hoffman, "Quantum-inspired design of a tunable broadband high-Q acoustic resonator," *arXiv*, 2024.

[3] R. P. Feynman, "Simulating physics with computers," *International Journal of Theoretical Physics*, vol. 21, no. 6-7, pp. 467–488, 1982.

[4] P. W. Shor, "Polynomial-Time Algorithms for Prime Factorization and Discrete Logarithms on a Quantum Computer," *SIAM Journal on Computing*, vol. 26, no. 5, pp. 1484–1509, 1997.

[5] T. D. Ladd, F. Jelezko, R. Laflamme, Y. Nakamura, C. Monroe, and J. L. O'Brien, "Quantum computers," *Nature*, vol. 464, no. 7285, pp. 45–53, 2010.

[6] D. P. DiVincenzo and IBM, "The Physical Implementation of Quantum Computation," *Fortschritte der Physik*, vol. 48, no. 9-11, pp. 771–783, 2000.

[7] E. Knill, "Quantum computing with realistically noisy devices," *Nature*, vol. 434, no. 7029, pp. 39–44, 2005.

[8] A. Kitaev, "Fault-tolerant quantum computation by anyons," *Annals of Physics*, vol. 303, pp. 2–30, 2003.

[9] S. Das Sarma, M. Freedman, and C. Nayak, "Majorana zero modes and topological quantum computation," *npj Quantum Information*, vol. 1, p. 15001, 2015.

[10] A. R. Akhmerov, "Topological quantum computation away from the ground state using Majorana fermions," *Physical Review B*, vol. 82, p. 020509, 2010.

[11] H. Røising, R. Ilan, T. Meng, S. Simon, and F. Flicker, "Finite temperature effects on Majorana bound states in chiral *p*-wave superconductors," *SciPost Physics*, vol. 6, p. 055, 2019.

[12] N. Read and D. Green, "Paired states of fermions in two dimensions with breaking of parity and time-reversal symmetries and the fractional quantum Hall effect," *Physical Review B*, vol. 61, pp. 10267–10297, 2000.

[13] S. Das Sarma, C. Nayak, and S. Tewari, "Proposal to stabilize and detect half-quantum vortices in strontium ruthenate thin films: Non-abelian braiding statistics of vortices in a $p_x + ip_y$ superconductor," *Physical Review B*, vol. 73, p. 220502, 2006.

[14] A. Stern and B. I. Halperin, "Proposed Experiments to Probe the Non-Abelian $\nu = 5/2$ Quantum Hall State," *Physical Review Letters*, vol. 96, no. 1, p. 016802, 2006.

[15] P. Bonderson, A. Kitaev, and K. Shtengel, "Detecting Non-Abelian Statistics in the $\nu = 5/2$ Fractional Quantum Hall State," *Physical Review Letters*, vol. 96, no. 1, p. 016803, 2006.

[16] Z.-T. Zhang and D. E. Liu, "Readout of Majorana bound states via Landau-Zener transition," *Physical Review B*, vol. 103, no. 19, p. 195401, 2021.

[17] C. K. McLauchlan and B. Béri, "Fermion-parity-based computation and its Majorana-zero-mode implementation," *Physical Review Letters*, vol. 128, no. 18, p. 180504, 2022.

[18] J. Schulenborg, S. Krøjer, M. Burrello, M. Leijnse, and K. Flensberg, "Detecting Majorana modes by readout of poisoning-induced parity flips," *Physical Review B*, vol. 107, no. 12, p. L121401, 2023.

[19] H. Xie, S. Yu, H. Mao, and J. Jin, "Majorana qubit readout by a point-contact detector under finite bias voltages." 2024.

[20] J. D. Sau and S. Das Sarma, "Capacitance-based fermion parity read-out and predicted Rabi oscillations in a Majorana nanowire." 2024.

[21] S. M. Albrecht, A. P. Higginbotham, M. Madsen, F. Kuemmeth, T. S. Jespersen, J. Nygård, P. Krogstrup, and C. M. Marcus, "Exponential protection of zero modes in Majorana islands," *Nature*, vol. 531, pp. 206–209, 2016.

[22] H. J. Suominen, M. Kjaergaard, A. R. Hamilton, J. Shabani, C. J. Palmstrøm, C. M. Marcus, and F. Nichele, "Zero-Energy Modes from Coalescing Andreev States in a Two-Dimensional Semiconductor-Superconductor Hybrid Platform," *Physical Review Letters*, vol. 119, p. 176805, 2017.

[23] C.-X. Liu, J. D. Sau, T. D. Stanescu, and S. Das Sarma, "Andreev bound states versus Majorana bound states in quantum dot-nanowire-superconductor hybrid structures: Trivial versus topological zero-bias conductance peaks," *Physical Review B*, vol. 96, p. 075161, 2017.

[24] S. S. Hegde, G. Yue, Y. Wang, E. Huemiller, D. J. Van Harlingen, and S. Vishveshwara, "A topological Josephson junction platform for creating, manipulating, and braiding Majorana bound states," *Annals of Physics*, vol. 423, p. 168326, 2020.

[25] K. Laubscher and J. D. Sau, "Detection of Majorana zero modes bound to Josephson vortices in planar S-TI-S junctions." 2024.

[26] G. Yue, C. Zhang, E. D. Huemiller, J. H. Montone, G. R. Arias, D. G. Wild, J. Y. Zhang, D. R. Hamilton, X. Yuan, X. Yao, D. Jain, J. Moon, M. Salehi, N. Koirala, S. Oh, and D. J. Van Harlingen, "Signatures of Majorana bound states in the diffraction patterns of extended superconductor–topological insulator–superconductor Josephson junctions," *Physical Review B*, vol. 109, no. 9, p. 094511, 2024.

[27] J. Schluck, E. Nikodem, A. Montag, A. Ziesen, M. Bagchi, F. Hassler, and Y. Ando, "Protected gap closing and reopening in topological-insulator Josephson junctions." 2024.

[28] L. Fu and C. L. Kane, "Superconducting Proximity Effect and Majorana Fermions at the Surface of a Topological Insulator," *Physical Review Letters*, vol. 100, p. 096407, 2008.

[29] N. Hao and J. Hu, "Topological quantum states of matter in iron-based superconductors: from concept to material realization," *National Science Review*, vol. 6, pp. 213–226, 2019.

[30] E. J. König and P. Coleman, "Crystalline-Symmetry-Protected Helical Majorana Modes in the Iron Pnictides," *Physical Review Letters*, vol. 122, p. 207001, 2019.

[31] D. Wang, L. Kong, P. Fan, H. Chen, S. Zhu, W. Liu, L. Cao, Y. Sun, S. Du, J. Schneeloch, R. Zhong, G. Gu, L. Fu, H. Ding, and H. J. Gao, "Evidence for Majorana bound states in an iron-based superconductor," *Science*, vol. 362, pp. 333–335, 2018.

[32] T. Machida, Y. Sun, S. Pyon, S. Takeda, Y. Kohsaka, T. Hanaguri, T. Sasagawa, and T. Tamegai, "Zero-energy vortex bound state in the superconducting topological surface state of Fe(Se,Te)," *Nature Materials*, vol. 18, pp. 811–815, 2019.

[33] L. Kong, S. Zhu, M. Papaj, H. Chen, L. Cao, H. Isobe, Y. Xing, W. Liu, D. Wang, P. Fan, Y. Sun, S. Du, J. Schneeloch, R. Zhong, G. Gu, L. Fu, H.-J. Gao, and H. Ding, "Half-integer level shift of vortex bound states in an iron-based superconductor," *Nature Physics*, vol. 15, no. 11, pp. 1181–1187, 2019.

[34] S. Zhu, L. Kong, L. Cao, H. Chen, M. Papaj, S. Du, Y. Xing, W. Liu, D. Wang, C. Shen, F. Yang, J. Schneeloch, R. Zhong, G. Gu, L. Fu, Y.-Y. Zhang, H. Ding, and H.-J. Gao, "Nearly quantized conductance plateau of vortex zero mode in an iron-based superconductor," *Science*, vol. 367, pp. 189–192, 2020.

[35] Q. Liu, C. Chen, T. Zhang, R. Peng, Y.-J. Yan, C.-H.-P. Wen, X. Lou, Y.-L. Huang, J.-P. Tian, X.-L. Dong, G.-W. Wang, W.-C. Bao, Q.-H. Wang, Z.-P. Yin, Z.-X. Zhao, and D.-L. Feng, "Robust and clean Majorana zero mode in the vortex core of high-temperature superconductor $(Li_{0.84}Fe_{0.16})$OHFeSe," *Physical Review X*, vol. 8, p. 041056, 2018.

[36] W. Liu, L. Cao, S. Zhu, L. Kong, G. Wang, M. Papaj, P. Zhang, Y.-B. Liu, H. Chen, G. Li, F. Yang, T. Kondo, S. Du, G.-H. Cao, S. Shin, L. Fu, Z. Yin, H.-J. Gao, and H. Ding, "A new Majorana platform in an Fe-As bilayer superconductor," *Nature Communications*, vol. 11, p. 5688, 2020.

[37] L. Kong, L. Cao, S. Zhu, M. Papaj, G. Dai, G. Li, P. Fan, W. Liu, F. Yang, X. Wang, S. Du, C. Jin, L. Fu, H.-J. Gao, and H. Ding, "Majorana zero modes in impurity-assisted vortex of LiFeAs superconductor," *Nature Communications*, vol. 12, p. 4146, 2021.

[38] C. Caroli, P. G. de Gennes, and J. Matricon, "Bound fermion states on a vortex line in a type II superconducor," *Physics Letters*, vol. 9, pp. 307–309, 1964.

[39] N. Hayashi, T. Isoshima, M. Ichioka, and K. Machida, "Low-Lying Quasiparticle Excitations around a Vortex Core in Quantum Limit," *Physical Review Letters*, vol. 80, no. 13, pp. 2921–2924, 1998.

[40] D. A. Ivanov, "Non-Abelian Statistics of Half-Quantum Vortices in p-Wave Superconductors," *Physical Review Letters*, vol. 86, no. 2, pp. 268–271, 2001.

[41] See Supplemental Material at https://arxiv.org/abs/1905.09792 for a table of Fe-based superconductors exhibiting MZMs; additional theoretical details including the derivation and solution of the radial BdG equation and the chiral limit; and additional experimental details including MFM sensitivity and noise floor, the circulating supercurrent, stray magnetic fields, and pinning forces associated with conventional vortices.

[42] A. Kremen, S. Wissberg, N. Haham, E. Persky, Y. Frenkel, and B. Kalisky, "Mechanical Control of Individual Superconducting Vortices," *Nano Letters*, vol. 16, pp. 1626–1630, 2016.

[43] J.-Y. Ge, V. N. Gladilin, J. Tempere, C. Xue, J. T. Devreese, J. Van de Vondel, Y. Zhou, and V. V. Moshchalkov, "Nanoscale assembly of superconducting vortices with scanning tunnelling microscope tip," *Nature Communications*, vol. 7, p. 13880, 2016.

[44] B. W. Gardner, J. C. Wynn, D. A. Bonn, R. Liang, W. N. Hardy, J. R. Kirtley, V. G. Kogan, and K. A. Moler, "Manipulation of single vortices in $YBa_2Cu_3O_{6.354}$ with a locally applied magnetic field," *Applied Physics Letters*, vol. 80, pp. 1010–1012, 2002.

[45] E. W. J. Straver, J. E. Hoffman, O. M. Auslaender, D. Rugar, and K. A. Moler, "Controlled manipulation of individual vortices in a superconductor," *Applied Physics Letters*, vol. 93, p. 172514, 2008.

[46] V. V. Dremov, S. Y. Grebenchuk, A. G. Shishkin, D. S. Baranov, R. A. Hovhannisyan, O. V. Skryabina, N. Lebedev, I. A. Golovchanskiy, V. I. Chichkov, C. Brun, T. Cren, V. M. Krasnov, A. A. Golubov, D. Roditchev, and V. S. Stolyarov, "Local Josephson vortex generation and manipulation with a Magnetic Force Microscope," *Nature Communications*, vol. 10, no. 1, p. 4009, 2019.

[47] X. Ma, C. J. O. Reichhardt, and C. Reichhardt, "Braiding Majorana fermions and creating quantum logic gates with vortices on a periodic pinning structure," *Physical Review B*, vol. 101, no. 2, p. 024514, 2020.

[48] P. Zhang, K. Yaji, T. Hashimoto, Y. Ota, T. Kondo, K. Okazaki, Z. Wang, J. Wen, G. D. Gu, H. Ding, and S. Shin, "Observation of topological superconductivity on the surface of an iron-based superconductor," *Science*, vol. 360, pp. 182–186, 2018.

[49] T. Hanaguri, S. Niitaka, K. Kuroki, and H. Takagi, "Unconventional *s*-Wave Superconductivity in Fe(Se,Te)," *Science*, vol. 328, pp. 474–476, 2010.

[50] J.-X. Yin, Z. Wu, J.-H. Wang, Z.-Y. Ye, J. Gong, X.-Y. Hou, L. Shan, A. Li, X.-J. Liang, X.-X. Wu, J. Li, C.-S. Ting, Z.-Q. Wang, J.-P. Hu, P.-H. Hor, H. Ding, and S. H. Pan, "Observation of a robust zero-energy bound state in iron-based superconductor Fe(Te,Se)," *Nature Physics*, vol. 11, pp. 543–546, 2015.

[51] H. Lohani, T. Hazra, A. Ribak, Y. Nitzav, H. Fu, B. Yan, M. Randeria, and A. Kanigel, "Band inversion and topology of the bulk electronic structure in $FeSe_{0.45}Te_{0.55}$," *Physical Review B*, vol. 101, p. 245146, 2020.

[52] H. Nielsen and M. Ninomiya, "The Adler-Bell-Jackiw anomaly and Weyl fermions in a crystal," *Physics Letters B*, vol. 130, pp. 389–396, 1983.

[53] R. Jackiw and P. Rossi, "Zero modes of the vortex-fermion system," *Nuclear Physics B*, vol. 190, pp. 681–691, 1981.

[54] C.-H. Lin, J. D. Sau, and S. Das Sarma, "Zero-bias conductance peak in Majorana wires made of semiconductor/superconductor hybrid structures," *Physical Review B*, vol. 86, p. 224511, 2012.

[55] G. Ben-Shach, A. Haim, I. Appelbaum, Y. Oreg, A. Yacoby, and B. I. Halperin, "Detecting Majorana modes in one-dimensional wires by charge sensing," *Physical Review B*, vol. 91, p. 045403, 2015.

[56] Z. Deng, E. Yenilmez, J. Leu, J. E. Hoffman, E. W. J. Straver, H. Dai, and K. A. Moler, "Metal-coated carbon nanotube tips for magnetic force microscopy," *Applied Physics Letters*, vol. 85, no. 25, pp. 6263–6265, 2004.

[57] T. R. Albrecht, P. Grütter, D. Horne, and D. Rugar, "Frequency modulation detection using high-Q cantilevers for enhanced force microscope sensitivity," *Journal of Applied Physics*, vol. 69, pp. 668–673, 1991.

[58] J. Schwenk, S. Kim, J. Berwanger, F. Ghahari, D. Walkup, M. R. Slot, S. T. Le, W. G. Cullen, S. R. Blankenship, S. Vranjkovic, H. J. Hug, Y. Kuk, F. J. Giessibl, and J. A. Stroscio, "Achieving μeV tunneling resolution in an in-operando scanning tunneling microscopy,

atomic force microscopy, and magnetotransport system for quantum materials research," *Review of Scientific Instruments*, vol. 91, p. 071101, 2020.

[59] A. Chaves, F. M. Peeters, G. A. Farias, and M. V. Milošević, "Vortex-vortex interaction in bulk superconductors: Ginzburg-Landau theory," *Physical Review B*, vol. 83, p. 054516, 2011.

[60] T. Barik and J. D. Sau, "Signatures of nontopological patches on the surface of topological insulators," *Physical Review B*, vol. 105, no. 3, p. 035128, 2022.

[61] I. P. Zhang, J. C. Palmstrom, H. Noad, L. Bishop-Van Horn, Y. Iguchi, Z. Cui, E. Mueller, J. R. Kirtley, I. R. Fisher, and K. A. Moler, "Imaging anisotropic vortex dynamics in FeSe," *Physical Review B*, vol. 100, p. 024514, 2019.

[62] F. Massee, P. O. Sprau, Y.-L. Wang, J. C. S. Davis, G. Ghigo, G. D. Gu, and W.-K. Kwok, "Imaging atomic-scale effects of high-energy ion irradiation on superconductivity and vortex pinning in Fe(Se,Te)," *Science Advances*, vol. 1, p. e1500033, 2015.

[63] G. Catelani, J. Koch, L. Frunzio, R. J. Schoelkopf, M. H. Devoret, and L. I. Glazman, "Quasiparticle Relaxation of Superconducting Qubits in the Presence of Flux," *Physical Review Letters*, vol. 106, p. 077002, 2011.

[64] C. Nayak, S. H. Simon, A. Stern, M. Freedman, and S. Das Sarma, "Non-Abelian anyons and topological quantum computation," *Reviews of Modern Physics*, vol. 80, pp. 1083–1159, 2008.

[65] M. Huefner, A. Pivonka, J. Kim, C. Ye, M. A. Blood-Forsythe, M. Zech, and J. E. Hoffman, "Microcantilever Q control via capacitive coupling," *Applied Physics Letters*, vol. 101, p. 173110, 2012.

[66] Y. Cao, V. Fatemi, A. Demir, S. Fang, S. L. Tomarken, J. Y. Luo, J. D. Sanchez-Yamagishi, K. Watanabe, T. Taniguchi, E. Kaxiras, R. C. Ashoori, and P. Jarillo-Herrero, "Correlated insulator behaviour at half-filling in magic-angle graphene superlattices," *Nature*, vol. 556, pp. 80–84, 2018.

[67] Y. Cao, V. Fatemi, S. Fang, K. Watanabe, T. Taniguchi, E. Kaxiras, and P. Jarillo-Herrero, "Unconventional superconductivity in magic-angle graphene superlattices," *Nature*, vol. 556, pp. 43–50, 2018.

[68] R. Bistritzer and A. H. MacDonald, "Moiré bands in twisted double-layer graphene," *Proceedings of the National Academy of Sciences*, vol. 108, pp. 12233–12237, 2011.

[69] G. Harari, M. A. Bandres, Y. Lumer, M. C. Rechtsman, Y. D. Chong, M. Khajavikhan, D. N. Christodoulides, and M. Segev, "Topological insulator laser: Theory," *Science*, vol. 359, p. eaar4003, 2018.

[70] M. A. Bandres, S. Wittek, G. Harari, M. Parto, J. Ren, M. Segev, D. N. Christodoulides, and M. Khajavikhan, "Topological insulator laser: Experiments," *Science*, vol. 359, p. eaar4005, 2018.

[71] J.-P. Xia, D. Jia, H.-X. Sun, S.-Q. Yuan, Y. Ge, Q.-R. Si, and X.-J. Liu, "Programmable coding acoustic topological insulator," *Advanced Materials*, vol. 30, p. 1805002, 2018.

[72] H. Pirie, S. Sadhuka, J. Wang, R. Andrei, and J. E. Hoffman, "Topological phononic logic," *Physical Review Letters*, vol. 128, p. 015501, 2022.

[73] Y. Yang, Y. Ge, R. Li, X. Lin, D. Jia, Y.-J. Guan, S.-Q. Yuan, H.-X. Sun, Y. Chong, and B. Zhang, "Demonstration of negative refraction induced by synthetic gauge fields," *Science Advances*, vol. 7, p. eabj2062, 2021.

[74] M. Dubois, C. Shi, X. Zhu, Y. Wang, and X. Zhang, "Observation of acoustic Dirac-like cone and double zero refractive index," *Nature Communications*, vol. 8, p. 14871, 2017.

[75] H. Tang, C. DeVault, S. A. Camayd-Muñoz, Y. Liu, D. Jia, F. Du, O. Mello, D. I. Vulis, Y. Li, and E. Mazur, "Low-loss zero-index materials," *Nano Letters*, vol. 21, pp. 914–920, 2021.

[76] F. Wu, T. Lovorn, E. Tutuc, and A. H. MacDonald, "Hubbard model physics in transition metal dichalcogenide moiré bands," *Physical Review Letters*, vol. 121, p. 026402, 2018.

[77] F. Wu, T. Lovorn, E. Tutuc, I. Martin, and A. H. MacDonald, "Topological insulators in twisted transition metal dichalcogenide homobilayers," *Physical Review Letters*, vol. 122, p. 086402, 2019.

[78] L. Xian, D. M. Kennes, N. Tancogne-Dejean, M. Altarelli, and A. Rubio, "Multiflat bands and strong correlations in twisted bilayer boron nitride: Doping-induced correlated insulator and superconductor," *Nano Letters*, vol. 19, pp. 4934–4940, 2019.

[79] K. L. Seyler, P. Rivera, H. Yu, N. P. Wilson, E. L. Ray, D. G. Mandrus, J. Yan, W. Yao, and X. Xu, "Signatures of moiré-trapped valley excitons in $MoSe_2/WSe_2$ heterobilayers," *Nature*, vol. 567, pp. 66–70, 2019.

[80] C. Jin, E. C. Regan, A. Yan, M. Iqbal Bakti Utama, D. Wang, S. Zhao, Y. Qin, S. Yang, Z. Zheng, S. Shi, K. Watanabe, T. Taniguchi, S. Tongay, A. Zettl, and F. Wang, "Observation of moiré excitons in WSe_2/WS_2 heterostructure superlattices," *Nature*, vol. 567, pp. 76–80, 2019.

[81] D. Pei, B. Wang, Z. Zhou, Z. He, L. An, S. He, C. Chen, Y. Li, L. Wei, A. Liang, J. Avila, P. Dudin, V. Kandyba, A. Giampietri, M. Cattelan, A. Barinov, Z. Liu, J. Liu, H. Weng, N. Wang, J. Xue, and Y. Chen, "Observation of Γ-valley moiré bands and emergent hexagonal lattice in twisted transition metal dichalcogenides," *Physical Review X*, vol. 12, p. 021065, 2022.

[82] J. Jung, A. Raoux, Z. Qiao, and A. H. MacDonald, "Ab initio theory of moiré superlattice bands in layered two-dimensional materials," *Physical Review B*, vol. 89, p. 205414, 2014.

[83] S. Carr, S. Fang, and E. Kaxiras, "Electronic-structure methods for twisted moiré layers," *Nature Reviews Materials*, vol. 5, pp. 748–763, 2020.

[84] S. Carr, D. Massatt, M. Luskin, and E. Kaxiras, "Duality between atomic configurations and Bloch states in twistronic materials," *Physical Review Research*, vol. 2, p. 033162, 2020.

[85] M. Angeli and A. H. MacDonald, "Γ valley transition metal dichalcogenide moiré bands," *Proceedings of the National Academy of Sciences*, vol. 118, p. e2021826118, 2021.

[86] H. Tang, S. Carr, and E. Kaxiras, "Geometric origins of topological insulation in twisted layered semiconductors," *Physical Review B*, vol. 104, p. 155415, 2021.

[87] S. M. Gardezi, H. Pirie, S. Carr, W. Dorrell, and J. E. Hoffman, "Simulating twistronics in acoustic metamaterials," *2D Materials*, vol. 8, p. 031002, 2021.

[88] W. Dorrell, H. Pirie, S. M. Gardezi, N. C. Drucker, and J. E. Hoffman, "Van der Waals metamaterials," *Physical Review B*, vol. 101, p. 121103, 2020.

[89] Y. Hashimoto and Y. Monnai, "Airborne ultrasound pulse amplification based on acoustic resonance switching," *Scientific Reports*, vol. 12, p. 18488, 2022.

[90] F. Kronowetter, M. Maeder, Y. K. Chiang, L. Huang, J. D. Schmid, S. Oberst, D. A. Powell, and S. Marburg, "Realistic prediction and engineering of high-Q modes to implement stable Fano resonances in acoustic devices," *Nature Communications*, vol. 14, p. 6847, 2023.

[91] F. Akbari-Farahani and S. Ebrahimi-Nejad, "From defect mode to topological metamaterials: A state-of-the-art review of phononic crystals & acoustic metamaterials for energy harvesting," *Sensors and Actuators A*, vol. 365, p. 114871, 2024.

[92] M. S. Luchansky and R. C. Bailey, "High-Q optical sensors for chemical and biological analysis," *Analytical Chemistry*, vol. 84, pp. 793–821, 2012.

[93] S. Kapfinger, T. Reichert, S. Lichtmannecker, K. Müller, J. J. Finley, A. Wixforth, M. Kaniber, and H. J. Krenner, "Dynamic acousto-optic control of a strongly coupled photonic molecule," *Nature Communications*, vol. 6, p. 8540, 2015.

[94] S. A. Tadesse and M. Li, "Sub-optical wavelength acoustic wave modulation of integrated photonic resonators at microwave frequencies," *Nature Communications*, vol. 5, p. 5402, 2014.

[95] N. Singh, M. Raval, A. Ruocco, and M. R. Watts, "Broadband 200-nm second-harmonic generation in silicon in the telecom band," *Light: Science & Applications*, vol. 9, p. 17, 2020.

[96] Y. Zhang, K. Zhong, X. Zhou, and H. K. Tsang, "Broadband high-Q multimode silicon concentric racetrack resonators for widely tunable Raman lasers," *Nature Communications*, vol. 13, p. 3534, 2022.

[97] S.-Y. Yu, X.-C. Sun, X. Ni, Q. Wang, X.-J. Yan, C. He, X.-P. Liu, L. Feng, M.-H. Lu, and Y.-F. Chen, "Surface phononic graphene," *Nature Materials*, vol. 15, pp. 1243–1247, 2016.

[98] J.-Q. Wang, Z.-D. Zhang, S.-Y. Yu, H. Ge, K.-F. Liu, T. Wu, X.-C. Sun, L. Liu, H.-Y. Chen, C. He, M.-H. Lu, and Y.-F. Chen, "Extended topological valley-locked surface acoustic waves," *Nature Communications*, vol. 13, p. 1324, 2022.

[99] Y. Achaoui, A. Khelif, S. Benchabane, L. Robert, and V. Laude, "Experimental observation of locally-resonant and Bragg band gaps for surface guided waves in a phononic crystal of pillars," *Physical Review B*, vol. 83, p. 104201, 2011.

[100] H. Kähler, D. Platz, and S. Schmid, "Surface acoustic wave coupling between micromechanical resonators," *Communications Physics*, vol. 5, p. 118, 2022.

[101] M. Oudich, G. Su, Y. Deng, W. Benalcazar, R. Huang, N. J. R. K. Gerard, M. Lu, P. Zhan, and Y. Jing, "Photonic analog of bilayer graphene," *Physical Review B*, vol. 103, p. 214311, 2021.

[102] H. Tang, B. Lou, F. Du, M. Zhang, X. Ni, W. Xu, R. Jin, S. Fan, and E. Mazur, "Experimental probe of twist angle–dependent band structure of on-chip optical bilayer photonic crystal," *Science Advances*, vol. 9, p. eadh8498, 2023.

[103] Y. Li, C. T. Chan, and E. Mazur, "Dirac-like cone-based electromagnetic zero-index metamaterials," *Light: Science & Applications*, vol. 10, p. 203, 2021.

[104] N. Marzari and D. Vanderbilt, "Maximally localized generalized wannier functions for composite energy bands," *Phys. Rev. B*, vol. 56, pp. 12847–12865, Nov 1997.

[105] T. Thonhauser and D. Vanderbilt, "Insulator/chern-insulator transition in the haldane model," *Phys. Rev. B*, vol. 74, p. 235111, Dec 2006.

[106] M. Z. Hasan and C. L. Kane, "Colloquium: Topological insulators," *Reviews of Modern Physics*, vol. 82, no. 4, pp. 3045–3067, 2010. RMP.

[107] J. E. Moore, "The birth of topological insulators," *Nature*, vol. 464, no. 7286, pp. 194–8, 2010.

[108] A. A. Soluyanov and D. Vanderbilt, "Wannier representation of F_2 topological insulators," *Phys. Rev. B*, vol. 83, p. 035108, Jan 2011.

[109] N. Marzari, A. A. Mostofi, J. R. Yates, I. Souza, and D. Vanderbilt, "Maximally localized wannier functions: Theory and applications," *Reviews of Modern Physics*, vol. 84, no. 4, pp. 1419–1475, 2012.

[110] G. Panati and A. Pisante, "Bloch bundles, marzari-vanderbilt functional and maximally localized wannier functions," *Communications in Mathematical Physics*, vol. 322, no. 3, pp. 835–875, 2013.

[111] B. Bradlyn, L. Elcoro, J. Cano, M. G. Vergniory, Z. Wang, C. Felser, M. I. Aroyo, and B. A. Bernevig, "Topological quantum chemistry," *Nature*, vol. 547, no. 7663, pp. 298–305, 2017.

[112] J. Cano, B. Bradlyn, Z. Wang, L. Elcoro, M. G. Vergniory, C. Felser, M. I. Aroyo, and B. A. Bernevig, "Topology of disconnected elementary band representations," *Phys Rev Lett*, vol. 120, no. 26, p. 266401, 2018.

[113] H. Xue, Y. Yang, F. Gao, Y. Chong, and B. Zhang, "Acoustic higher-order topological insulator on a kagome lattice," *Nat Mater*, vol. 18, no. 2, pp. 108–112, 2019.

[114] Y. Xu, L. Elcoro, G. Li, Z.-D. Song, N. Regnault, Q. Yang, Y. Sun, S. Parkin, C. Felser, and B. A. Bernevig, "Three-Dimensional Real Space Invariants, Obstructed Atomic Insulators and A New Principle for Active Catalytic Sites," *arXiv e-prints*, p. arXiv:2111.02433, Nov. 2021.

[115] G. Li, Y. Xu, Z. Song, Q. Yang, U. Gupta, V. Sü{eta}, Y. Sun, P. Sessi, S. S. P. Parkin, B. A. Bernevig, and C. Felser, "Obstructed surface states as the origin of catalytic activity in inorganic heterogeneous catalysts," *arXiv e-prints*, p. arXiv:2111.02435, Nov. 2021.

[116] D. Călugăru, Y. Jiang, H. Guo, S. Sajan, Y. Wang, H. Hu, J. Yu, B. A. Bernevig, F. de Juan, and M. M. Ugeda, "Probing the Quantized Berry Phases in 1H-$NbSe_2$ Using Scanning Tunneling Microscopy," *arXiv e-prints*, p. arXiv:2501.09063, Jan. 2025.

[117] J. G. Checkelsky, B. A. Bernevig, P. Coleman, Q. Si, and S. Paschen, "Flat bands, strange metals and the kondo effect," *Nature Reviews Materials*, vol. 9, no. 7, pp. 509–526, 2024.

[118] "Discovery of a single-band mott insulator in a van der waals flat-band compound," *Phys. Rev. X*, vol. 13, p. 041049, Dec 2023.

[119] S. Xia, A. Ramachandran, S. Xia, D. Li, X. Liu, L. Tang, Y. Hu, D. Song, J. Xu, D. Leykam, S. Flach, and Z. Chen, "Unconventional flatband line states in photonic lieb lattices," *Physical Review Letters*, vol. 121, no. 26, p. 263902, 2018. PRL.

[120] M. Li, D. Zhirihin, M. Gorlach, X. Ni, D. Filonov, A. Slobozhanyuk, A. Alù, and A. B. Khanikaev, "Higher-order topological states in photonic kagome crystals with long-range interactions," *Nature Photonics*, vol. 14, no. 2, pp. 89–94, 2020.

[121] S. M. Gardezi, H. Pirie, S. Carr, W. Dorrell, and J. E. Hoffman, "Simulating twistronics in acoustic metamaterials," *2d materials*, vol. 8, no. 3, p. 31002, 2021.

[122] H. Tang, F. Du, S. Carr, C. DeVault, O. Mello, and E. Mazur, "Modeling the optical properties of twisted bilayer photonic crystals," *Light Sci Appl*, vol. 10, no. 1, p. 157, 2021.

[123] Y.-X. Shen, Y.-G. Peng, P.-C. Cao, J. Li, and X.-F. Zhu, "Observing localization and delocalization of the flat-band states in an acoustic cubic lattice," *Phys. Rev. B*, vol. 105, p. 104102, Mar 2022.

[124] P. Karki and J. Paulose, "Non-singular and singular flat bands in tunable phononic metamaterials," *Phys. Rev. Res.*, vol. 5, p. 023036, Apr 2023.

[125] L. Song, S. Gao, J. Ma, L. Tang, D. Song, Y. Li, and Z. Chen, "Multiple flatbands and localized states in photonic super-kagome lattices," *Optics Letters*, vol. 48, no. 22, pp. 5947–5950, 2023.

[126] Z.-D. Zhang, M.-H. Lu, and Y.-F. Chen, "Twist-angle-induced boundary-obstructed topological insulator on elastic kagome metamaterials," *Physical Review Applied*, vol. 20, no. 5, p. 054002, 2023. PRAPPLIED.

[127] W. Zhu, H. Zou, Y. Ge, Y. Wang, Z. Cheng, B.-b. Wang, S.-q. Yuan, H.-x. Sun, H. Xue, and B. Zhang, "Flatbands from Bound States in the Continuum for Orbital Angular Momentum Localization," *ArXiv*, 2024.

[128] Z. Chen, Y. B. Chong, K. M. Lim, and H. P. Lee, "Reconfigurable 3d printed acoustic metamaterial chamber for sound insulation," *International Journal of Mechanical Sciences*, vol. 266, p. 108978, 2024.

[129] R. Emanuele, F. Bellinzoni, and F. Braghin, "Creating compact localized modes for robust sound transport via singular flat band engineering," *ArXiv*, 2024.

[130] Y. Tang, B. Liang, X. Zhu, and S. Lin, "Systematic design and experimental realization of multiplexed acoustic double-zero-index metamaterials," *Physical review applied*, vol. 21, no. 3, 2024.

[131] M. Oudich, X. Kong, T. Zhang, C. Qiu, and Y. Jing, "Engineered moiré photonic and phononic superlattices," *Nature Materials*, vol. 23, no. 9, pp. 1169–1178, 2024.

[132] M. M. Samak and O. R. Bilal, "Direct observation of all-flat bands phononic metamaterials," *Physical review letters*, vol. 133, no. 26, 2024.

[133] W. A. Benalcazar, B. A. Bernevig, and T. L. Hughes, "Quantized electric multipole insulators," *Science*, vol. 357, no. 6346, pp. 61–66, 2017.

[134] M. Serra-Garcia, V. Peri, R. Susstrunk, O. R. Bilal, T. Larsen, L. G. Villanueva, and S. D. Huber, "Observation of a phononic quadrupole topological insulator," *Nature*, vol. 555, no. 7696, pp. 342–345, 2018.

[135] C. W. Peterson, W. A. Benalcazar, T. L. Hughes, and G. Bahl, "A quantized microwave quadrupole insulator with topologically protected corner states," *Nature*, vol. 555, no. 7696, pp. 346–350, 2018.

[136] W. P. Su, J. R. Schrieffer, and A. J. Heeger, "Solitons in polyacetylene," *Physical Review Letters*, vol. 42, no. 25, pp. 1698–1701, 1979. PRL.

[137] Y. Xu, L. Elcoro, Z.-D. Song, M. G. Vergniory, C. Felser, S. S. P. Parkin, N. Regnault, J. L. Mañes, and B. A. Bernevig, "Filling-enforced obstructed atomic insulators," *Physical Review B*, vol. 109, no. 16, p. 165139, 2024. PRB.

[138] D. Vanderbilt and R. D. King-Smith, "Electric polarization as a bulk quantity and its relation to surface charge," *Phys. Rev. B*, vol. 48, pp. 4442–4455, Aug 1993.

[139] R. D. King-Smith and D. Vanderbilt, "Theory of polarization of crystalline solids," *Phys. Rev. B*, vol. 47, pp. 1651–1654, Jan 1993.

[140] M. V. Berry, "Quantal phase factors accompanying adiabatic changes," *Proceedings of the Royal Society of London. A. Mathematical and Physical Sciences*, vol. 392, no. 1802, pp. 45–57, 1984.

[141] J. E. Moore and L. Balents, "Topological invariants of time-reversal-invariant band structures," *Physical Review B*, vol. 75, no. 12, 2007.

[142] K. Y. Steven M. Girvin, *Modern Condensed Matter Physics*. Cambrdige University Press, 2019.

[143] M. Xiao, W.-J. Chen, W.-Y. He, and C. T. Chan, "Synthetic gauge flux and weyl points in acoustic systems," *Nature physics*, vol. 11, no. 11, pp. 920–924, 2015.

[144] Z. Yang and B. Zhang, "Acoustic type-ii weyl nodes from stacking dimerized chains," *Physical Review Letters*, vol. 117, no. 22, 2016.

[145] Z. Yang, F. Gao, Y. Yang, and B. Zhang, "Strain-induced gauge field and landau levels in acoustic structures," *Physical review letters*, vol. 118, no. 19, pp. 194301–194301, 2017.

[146] B.-Q. Wu, Z.-K. Lin, L.-W. Wang, and J.-H. Jiang, "Observation of a *p*-orbital higher-order topological insulator phase in puckered lattice acoustic metamaterials," *Physical Review B*, vol. 109, no. 20, p. 205136, 2024. PRB.

[147] D. L. Bergman, C. Wu, and L. Balents, "Band touching from real-space topology in frustrated hopping models," *Phys. Rev. B*, vol. 78, p. 125104, Sep 2008.

[148] T. Szabo and A. Slobodnik, "The Effect of Diffraction on the Design of Acoustic Surface Wave Devices," *IEEE Transactions on Sonics and Ultrasonics*, vol. 20, no. 3, pp. 240–251, 1973.

[149] S. Mohammadi, A. A. Eftekhar, W. D. Hunt, and A. Adibi, "High-Q micromechanical resonators in a two-dimensional phononic crystal slab," *Applied Physics Letters*, vol. 94, no. 5, p. 051906, 2009.

[150] S. A. Tadesse and M. Li, "Sub-optical wavelength acoustic wave modulation of integrated photonic resonators at microwave frequencies," *Nature Communications*, vol. 5, no. 1, p. 5402, 2014.

[151] D. Zhu, L. Shao, M. Yu, R. Cheng, B. Desiatov, C. J. Xin, Y. Hu, J. Holzgrafe, S. Ghosh, A. Shams-Ansari, E. Puma, N. Sinclair, C. Reimer, M. Zhang, and M. Lončar, "Integrated photonics on thin-film lithium niobate," *Advances in Optics and Photonics*, vol. 13, no. 2, p. 242, 2021.

[152] L. Shao, S. Maity, L. Zheng, L. Wu, A. Shams-Ansari, Y.-I. Sohn, E. Puma, M. Gadalla, M. Zhang, C. Wang, E. Hu, K. Lai, and M. Lončar, "Phononic band structure engineering for high-Q gigahertz surface acoustic wave resonators on lithium niobate," *Physical Review Applied*, vol. 12, p. 014022, 2019.

[153] M. V. Gustafsson, P. V. Santos, G. Johansson, and P. Delsing, "Local probing of propagating acoustic waves in a gigahertz echo chamber," *Nature Physics*, vol. 8, no. 4, pp. 338–343, 2012.

[154] M. V. Gustafsson, T. Aref, A. F. Kockum, M. K. Ekström, G. Johansson, and P. Delsing, "Propagating phonons coupled to an artificial atom," *Science*, vol. 346, no. 6206, pp. 207–211, 2014.

[155] K. J. Satzinger, Y. P. Zhong, H.-S. Chang, G. A. Peairs, A. Bienfait, M.-H. Chou, A. Y. Cleland, C. R. Conner, . Dumur, J. Grebel, I. Gutierrez, B. H. November, R. G. Povey, S. J. Whiteley, D. D. Awschalom, D. I. Schuster, and A. N. Cleland, "Quantum control of surface acoustic-wave phonons," *Nature*, vol. 563, no. 7733, pp. 661–665, 2018.

[156] Y. Chu, P. Kharel, W. H. Renninger, L. D. Burkhart, L. Frunzio, P. T. Rakich, and R. J. Schoelkopf, "Quantum acoustics with superconducting qubits," *Science*, vol. 358, no. 6360, pp. 199–202, 2017.

[157] J. Lu, C. Qiu, L. Ye, X. Fan, M. Ke, F. Zhang, and Z. Liu, "Observation of topological valley transport of sound in sonic crystals," *Nature Physics*, vol. 13, pp. 369–374, 2017.

[158] V. Peri, Z.-D. Song, M. Serra-Garcia, P. Engeler, R. Queiroz, X. Huang, W. Deng, Z. Liu, B. A. Bernevig, and S. D. Huber, "Experimental characterization of fragile topology in an acoustic metamaterial," *Science*, vol. 367, no. 6479, pp. 797–800, 2020.

[159] X. Ni, M. Weiner, A. Alù, and A. B. Khanikaev, "Observation of higher-order topological acoustic states protected by generalized chiral symmetry," *Nature Materials*, vol. 18, no. 2, pp. 113–120, 2019.

[160] Q. Wei, X. Zhang, W. Deng, J. Lu, X. Huang, M. Yan, G. Chen, Z. Liu, and S. Jia, "Higher-order topological semimetal in acoustic crystals," *Nature Materials*, vol. 20, no. 6, pp. 812–817, 2021.

[161] M. Serra-Garcia, V. Peri, R. Süsstrunk, O. R. Bilal, T. Larsen, L. G. Villanueva, and S. D. Huber, "Observation of a phononic quadrupole topological insulator," *Nature*, vol. 555, pp. 342–345, 2018.

[162] Q. Zhang, D. Lee, L. Zheng, X. Ma, S. I. Meyer, L. He, H. Ye, Z. Gong, B. Zhen, K. Lai, and A. T. C. Johnson, "Gigahertz topological valley Hall effect in nanoelectromechanical phononic crystals," *Nature Electronics*, vol. 5, pp. 157–163, 2022.

[163] Z.-D. Zhang, S.-Y. Yu, H. Ge, J.-Q. Wang, H.-F. Wang, K.-F. Liu, T. Wu, C. He, M.-H. Lu, and Y.-F. Chen, "Topological Surface Acoustic Waves," *Physical Review Applied*, vol. 16, no. 4, p. 044008, 2021.

[164] D. R. Oliver, A. Pu, D. J. Thomson, and G. E. Bridges, "Heterodyne electrostatic imaging of polarization due to a surface acoustic wave," *Applied Physics Letters*, vol. 79, no. 22, pp. 3729–3731, 2001.

[165] T. Hesjedal and G. Behme, "High-resolution imaging of surface acoustic wave scattering," *Applied Physics Letters*, vol. 78, no. 13, pp. 1948–1950, 2001.

[166] I. Yahyaie, D. A. Buchanan, G. E. Bridges, D. J. Thomson, and D. R. Oliver, "High-resolution imaging of gigahertz polarization response arising from the interference of reflected surface acoustic waves," *IEEE Transactions on Ultrasonics, Ferroelectrics and Frequency Control*, vol. 59, no. 6, pp. 1212–1218, 2012.

[167] J. V. Sánchez-Pérez, D. Caballero, R. Mártinez-Sala, C. Rubio, J. Sánchez-Dehesa, F. Meseguer, J. Llinares, and F. Gálvez, "Sound Attenuation by a Two-Dimensional Array of Rigid Cylinders," *Physical Review Letters*, vol. 80, no. 24, pp. 5325–5328, 1998.

[168] D. Torrent, D. Mayou, and J. Sánchez-Dehesa, "Elastic analog of graphene: Dirac cones and edge states for flexural waves in thin plates," *Physical Review B*, vol. 87, no. 11, p. 115143, 2013.

[169] J. G. Bednorz and K. A. Müller, "Possible highTc superconductivity in the Ba–La–Cu–O system," *Zeitschrift für Physik B Condensed Matter*, vol. 64, no. 2, pp. 189–193, 1986.

[170] T. Neupert, M. M. Denner, J.-X. Yin, R. Thomale, and M. Z. Hasan, "Charge order and superconductivity in kagome materials," *Nature Physics*, vol. 18, pp. 137–143, 2022.

[171] H. Zhao, H. Li, B. R. Ortiz, S. M. L. Teicher, T. Park, M. Ye, Z. Wang, L. Balents, S. D. Wilson, and I. Zeljkovic, "Cascade of correlated electron states in the kagome superconductor CsV_3Sb_5," *Nature*, vol. 599, pp. 216–221, 2021.

[172] Y.-X. Jiang, J.-X. Yin, M. M. Denner, N. Shumiya, B. R. Ortiz, G. Xu, Z. Guguchia, J. He, M. S. Hossain, X. Liu, J. Ruff, L. Kautzsch, S. S. Zhang, G. Chang, I. Belopolski, Q. Zhang, T. A. Cochran, D. Multer, M. Litskevich, Z.-J. Cheng, X. P. Yang, Z. Wang, R. Thomale, T. Neupert, S. D. Wilson, and M. Z. Hasan, "Unconventional chiral charge order in kagome superconductor KV_3Sb_5," *Nature Materials*, vol. 20, pp. 1353–1357, 2021.

[173] B. R. Ortiz, S. M. L. Teicher, Y. Hu, J. L. Zuo, P. M. Sarte, E. C. Schueller, A. M. M. Abeykoon, M. J. Krogstad, S. Rosenkranz, R. Osborn, R. Seshadri, L. Balents, J. He, and S. D. Wilson, "CsV3Sb5: A Z2 Topological Kagome Metal with a Superconducting Ground State," *Physical Review Letters*, vol. 125, no. 24, p. 247002, 2020.

[174] J. Yang, X. Yi, Z. Zhao, Y. Xie, T. Miao, H. Luo, H. Chen, B. Liang, W. Zhu, Y. Ye, J.-Y. You, B. Gu, S. Zhang, F. Zhang, F. Yang, Z. Wang, Q. Peng, H. Mao, G. Liu, Z. Xu, H. Chen, H. Yang, G. Su, H. Gao, L. Zhao, and X. J. Zhou, "Observation of flat band, Dirac nodal lines and topological surface states in Kagome superconductor CsTi3Bi5," *Nature Communications*, vol. 14, no. 1, p. 4089, 2023.

[175] H. W. S. Arachchige, W. R. Meier, M. Marshall, T. Matsuoka, R. Xue, M. A. McGuire, R. P. Hermann, H. Cao, and D. Mandrus, "Charge Density Wave in Kagome Lattice Intermetallic ScV6Sn6," *Physical Review Letters*, vol. 129, no. 21, p. 216402, 2022.

[176] Y. Hu, J. Ma, Y. Li, Y. Jiang, D. J. Gawryluk, T. Hu, J. Teyssier, V. Multian, Z. Yin, S. Xu, S. Shin, I. Plokhikh, X. Han, N. C. Plumb, Y. Liu, J.-X. Yin, Z. Guguchia, Y. Zhao, A. P. Schnyder, X. Wu, E. Pomjakushina, M. Z. Hasan, N. Wang, and M. Shi, "Phonon promoted charge density wave in topological kagome metal ScV6Sn6," *Nature Communications*, vol. 15, no. 1, p. 1658, 2024.

[177] M. R. H. Lima, de Crasto and E. S. Morell, "Double flat bands in kagome twisted bilayers," *Physical Review B*, vol. 100, p. 155421, 2019.

[178] M. Yankowitz, J. Jung, E. Laksono, N. Leconte, B. L. Chittari, K. Watanabe, T. Taniguchi, S. Adam, D. Graf, and C. R. Dean, "Dynamic band-structure tuning of graphene moiré superlattices with pressure," *Nature*, vol. 557, no. 7705, pp. 404–408, 2018.

[179] M. Yankowitz, S. Chen, H. Polshyn, Y. Zhang, K. Watanabe, T. Taniguchi, D. Graf, A. F. Young, and C. R. Dean, "Tuning superconductivity in twisted bilayer graphene," *Science*, vol. 363, no. 6431, pp. 1059–1064, 2019.

[180] G. Tarnopolsky, A. J. Kruchkov, and A. Vishwanath, "Origin of Magic Angles in Twisted Bilayer Graphene," *Physical Review Letters*, vol. 122, no. 10, p. 106405, 2019.